The Reuse of High-Density Polyethylene (HDPE) Plastic Wastes and their Usage with Cerium Dioxide (CeO_2) as New Polymer Nanocomposites

DELİA TERESA SPONZA, RUKİYE ÖZTEKİN *
[a] Department of Environmental Engineering
Dokuz Eylül University
Tınaztepe Campus, 35160 Buca/Izmir,
TURKEY

**Corresponding Author*

Abstract: A high density polyethylene (HDPE) plastic was reused and it was used together with cerium dioxide (CeO_2) to photodegrade the Roxarsone (ROX, 4-hydroxy-3-nitrophenylarsonic acid). The microstructure of the HPDE/CeO_2 polymer nanocomposite was characterized by scanning electron microscopy (SEM) analysis, energy In the sunlight power (20-100 W/m^2), photooxidation time (10 – 100 min), pH (2-10), temperature (10^{o}C-40^{o}C), HDPE nanocomposites (NCs) concentrations (100-1600 mg/l), CeO_2 concentrations (2.5-18 mg/l) and the ratios of HDPE to CeO_2 (37.5-100), HDPE/CeO_2 NCs concentration (200-2400 mg/l) on the photodegradation yields of ROX was investigated. The surface properties of the HDPE/CeO_2 NCs was investigated by the XRD, SEM and FTIR analysis. For maximum photodegradation yields of ROX (99%) the optimum operational conditions were 60 W/m^2 sunlight power, pH=4.0, 40^{o}C, at 8 mg/l CeO_2 nanoparticles (NPs), at 300 mg/l HDPE concentration, at a HDPE TO CeO_2 ratio of 37.5, at 800 mg/l ROX concentration, after 30 min photodegradation duration, respectively. ROX was photodegraded according to Hinshelwood Kinetic with a reaction kinetic constant of k = 12.349 x 10^{-4} min^{-1}. EDS analysis showed that Ce and O were distributed on the surface and CeO_2 particles existed in the HDPE matrix. According to SEM analyses the aging treatment increased the adhesive wear level on the HDPE/CeO_2 NCs by leading to the increase of coefficients of friction (COF). XRD results showed that the characteristic peaks of the HDPE without aging were higher, and the height of the characteristic peak decreased after aging treatment. Therefore, the crystallinity of HDPE decreased, and showed that the fracture of internal molecular chain increased after aging treatment.

Key-Words: - Cerium dioxide (CeO_2); High-density polyethylene (HDPE); 4-Hydroxy-3-nitrophenylarsonic acid; Nanocomposites; Recycling; Reuse; Roxarsone (ROX); Photodegradation; Plastic Wastes; Polymer.

Received: April 15, 2026. Revised: May 19, 2026. Accepted: July 13, 2026. Published: November 19, 2026.

1 Introduction

High-density polyethylene (HDPE) polymer is one of the largest contributors to plastic wastes causing detrimental effects on various sectors of society, and is not biodegradable in nature. In the first stage, river sand and a recycled HDPE as a binder were used to manufacture eco-friendly plastic sand bricks with various sand (s): plastic (p) ratios, [1].

Unfortunately, the disposal of plastic waste presents significant environmental problems as it is non-biodegradable and can release toxic gases when incinerated, contributing to air pollution and posing a risk to humans, [2], [3].

Therefore, reuse of plastic waste is an option to protect and sustain future generations, [4]. With limited land space available for landfilling, incorporating HDPE plastic waste in the manufacturing of construction material presents a viable solution to the disposal problem, [5]. The advancement from non-renewable construction materials towards eco-friendly materials is gaining momentum, aligning with the concept of a circular economy (CE) and the pursuit of Sustainable Development Goals (SDGs).

HDPE or polyethylene high-density (PEHD) is a thermoplastic polymer produced from the monomer ethylene. It is sometimes called "alkathene" or "polythene" when used for HDPE pipes. With a high strength-to-density ratio, HDPE is used in the production of plastic bottles, corrosion-resistant piping, geomembranes and plastic lumber.

HDPE is a thermoplastic polymer derived from petroleum with a generalized chemical formula $(C_2H_4)_n$. The HDPE formula represents the repeating monomer unit of ethylene and forms a polyethylene (PE) molecular chain. HDPE is distinct from other

forms of PE in that its side chain branching frequency is lower than other PE types, where HDPE is commonly referred to as a "linear" chain.

The HDPE linear chain is represented in the Fig. 1:

* Figure 1 can be found in the Appendix section.

HDPE can be found everywhere because it is strong, lightweight, and highly resistant to chemicals, it is one of the most widely manufactured plastics in the world.

It is found at several major categories given below:

1. Household & Kitchen Items:
   - Food & Beverage Packaging: Milk jugs, juice cartons, water gallons, and squeeze bottles (like chocolate syrup or vinegar).
   - Pantry Liners: The crinkly, moisture-resistant bags found inside cereal boxes and cracker boxes.
   - Kitchen Tools: Heavy-duty cutting boards and food storage containers.
   - Disposal: Puncture-resistant trash bags and shopping grocery bags.
2. Bathroom & Cleaning Products:
   - Personal Care: Shampoo, conditioner, body wash, and cosmetic lotion bottles.
   - Chemical Cleaners: Heavy-duty laundry detergent jugs, bleach bottles, and household chemical spray containers.
3. Around the House & Outdoors:
   - Home Infrastructure: Corrosion-resistant water pipes, natural gas distribution lines, and sewage pipes.
   - Gardening & Patio: Plastic lumber decking, patio chairs, flowerpots, recycling bins, and large trash cans.
   - Recreation: Playground equipment, toys, hard hats, and even the slick bases of snowboards.
4. Industrial & Specialized Settings:
   - Logistics: Commercial shipping pallets, plastic crates, and massive chemical drums.
   - Automotive: Vehicle fuel tanks and inner cable protectors.
   - Medical: Pharmaceutical pill bottles and even specialized structural implants used in plastic surgery.

This is a highly simplistic overview of the process, as polymerization organic chemistry is much more detailed (and organic chemists still do not fully understand the reaction mechanism!). Regardless, note that HDPE is made from petroleum and is processed using catalysts to form long, linear, and dense polyethylene (PE) now known as HDPE.

The properties shown below illustrates the utilization items of recycled and raw HDPE:

The incorporation of recycled HDPE plastics known for their high mechanical strength, [6], into building and construction, [2], is one of the options for a safe, efficient and sustainable solution for waste disposal and plastic pollution, [4]. The incorporation of plastic as an alternative material has the potential to address the high building costs in South Africa, in Nigeria, and in Malaysia, [2]. Hence, this shows that the inclusion of plastic waste in building materials is beneficial to the construction industry.

The HDPE has significant applications as an engineering material due to its excellent properties such as very low relative permittivity (er ¼ 2.6 at 1 MHz), low dielectric loss (tan d ¼ 104 at 1 MHz), good chemical resistance, and insulating properties. HDPE materials appear in many places in our daily lives. The fact that it can be produced in various properties according to the place of use increases the use of these materials. One of the advantages of HDPE materials are high chemical resistance compared to metals. On the other hand, some change in mechanical properties can be observed as a result of thermal effects. Identifying and revealing these properties are also of great importance. The effect of boron nitride content, on the particle size of HDPE and temperature on the thermal conductivity of HDPEs were investigated, [7]. The effect of material parameters and processing conditions on the foam morphologies and mechanical properties of HDPE clay NCs were studied, [8]. Ceria possess good dielectric and thermal properties. It has a relative permittivity of 23, dielectric loss less than 0.0001 at 7 GHz and polymer NCs. The possibility of using CeO_2-filled HDPE as a substrate material for high frequency applications has been explored for the first time. The experimental results are compared with well-known theoretical predictions, [8].

In the shipbuilding industry, HDPE is a kind of common water-lubricated bearing material which can enhance navigation safety, [9], [10]. However, the HDPE material will be aged after a long time service especially under high temperature conditions, which have negative effects on the operating system. For instance, aging phenomenon will damage the structure of internal molecular chain of HDPE and weaken the mechanical properties, which leads to poor tribological properties in the end, [11], [12], [13]. These researchs show that external factors such as temperature and humidity can accelerate the aging of HDPE after high temperature treatment of the molecular chain of HDPE will break. This affect its relative molecular weight and crosslinking degree thereby the mechanical properties including strength and hardness were weakene. As a result this negative influence, decrease its working performance, [14]. Various nano-fillers have been used in modification of HDPE matrix material, and tried to improve its anti-aging properties and also facilitated its application in the industrial field.

Fluoropolymeric materials are the most desirable polymer matrix for flexible substrate fabrication due to their superior high electrical properties and excellent temperature and solvent resistance. Among frequency fluropolymers polytetrafluoroethylene (PTFE) is the most preferred host matrix for substrate applications due to its low permitivity, low loss, and relatively high service temperature. The disadvantages are the difficulty in processing the PTFE—based laminates and the relatively high filler loading required for preparing dimensionally stable PTFE composites, [6]. The use of HDPE by the communication industry as the dielectric in submarine cables encouraged us to investigate the effect of CeO_2 filler loading on the microwave dielectric properties of HDPE-CeO_2 NCs. Polyethylene (PE) is a nonpolar polymer improving the properties of HDPE composites due to its semicrystalline structure.

Roxarsone (ROX, 4-hydroxy-3-nitrophenylarsonic acid) is an organoarsenical chemical and is widely used in the poultry industry as a feed additive to improve the feed efficiency by preventing the coccidial intestinal parasites, [15], [16]. Most of ROX in the feed is excreted to poultry litter. It has been reported that 29.80 mg/kg of total arsenic concentration was detected in the poultry litter, [16], [17].

ROX could be photodegraded in the aquatic environment, such as in poultry litter leachates and surface water, [18], [19], but ROX photodegradation behaviour has not been fully understood. In general, the photodegradation of organic contaminants can be divided into two main types: direct photolysis and indirect photolysis. Organic contaminants can be directly photodegraded through the absorbance of photons and/or indirectly photodegraded by reactive oxygen species (ROS) [OH or singlet oxygen and/or dioxidene ($^1O_2$)] and other kinds of reactive radicals, [17], [20]. Photodegradation is affected by water quality and environmental conditions, [16]. Light intensity and temperature promoted photodegradation efficiency, while dissolved organic matter (DOM) enhanced or inhibited the photodegradation of organic contaminants,[15], [16]. Therefore, investigating the factors affecting the ROX photodagradation would improve the understanding of ROX photodegradation behaviour. ROX, an organoarsenic feed additive, can be discharged into aquatic environment and photodegraded into more toxic inorganic arsenics.

In the study performed by Acuña et al., [21], an efficient photodegradation of ROX was achieved by using synthesized zinc oxide (ZnO) nanoplates under UV light irradiation. ROX's degradation by-products such as As(III), As(V) were analysed. Photocatalytic degradation of ROX leads to mineralization as CO_2 and As(V).

In the study by Meng et al., [22], ROX was photodegraded into more toxic inorganic arsenics, causing arsenic pollution. The results showed that ROX in the aquatic environment was degraded to inorganic As(III) and As(V) under light irradiation. The degradation efficiency was enhanced by 25% with the increase of light intensity from 300 $\mu W/cm^2$ to 800 $\mu W/cm^2$ via indirect photolysis. The photodegradation of ROX was significantly influenced by temperature and Nitrate ion (NO_3^-), but sulfate, carbonate, and chlorate ions had a negligible effect on ROX degradation. DOM in the solution inhibited the photodegradation. ROX photodegradation was mainly mediated by reactive oxygen species (in the form of single oxygen, $^1O_2$) generated through ROX self-sensitization under irradiation.

Bednar et al., [23], found that the toxicity of roxarsone is less than that of inorganic arsenic, roxarsone can degrade, biotically and abiotically, to produce more toxic inorganic forms of arsenic, such as arsenite and arsenate. Experiments showed that arsenite can be cleaved photolytically from the roxarsone moiety at pH 4.0–8.0 and that the degradation rate increases with increasing pH. Furthermore, the rate of photodegradation increases with nitrate and natural organic matter concentration, reactants that are commonly found in poultry-litter-water leachates while photochemical reactions rapidly oxidize the cleaved arsenite to arsenate. The formation of arsenate is not entirely undesirable, because it is less mobile in soil systems and less toxic than arsenite.

Highly effective oxidation of roxarsone by ferrate and simultaneous arsenic removal within situ formed ferric nanoparticles in the study performed by Yang et al., [24].

As aforementioned, photo degradation, [23], [25], [26], have been investigated for the removal of ROX in aqueous solution. Adsorbents such as Fe_3O_4@RGO nanocomposite, [24], Fe-Mn binary oxides, [25], and iron and aluminium oxides, [27], have shown great results for ROX removal. However, organoarsenic compounds are difficult to be removed through adsorption process as compared with inorganic arsenic, and the time to achieve desired adsorption equilibrium is normally more than 5h.

The CeO_2 and other nanocomposites used in the photodegradation of ROX cause to production of more toxic metabolites than ROX photoremoval and provide low photodegradation or adsorption yields.

Rao and Khan, [28], used HDPE with clay based nanocomposites to remove flame retardant organics. Nanoclay has a large surface area and thus, smaller filler loadings can be used to achieve adequate

photocalalysis to remove the fire retardants. The major challenge of blending these nanoparticles with HDPE is their dispersion in the matrix. It has been envisaged that flame retardancy of polymer-clay nanocomposites are significantly improved with reduced filler loadings.

Therefore, in this study HDPE/CeO_2 nanocomposite was used to photodegrade the ROX chemical under sunlight. In this study, the effects of increasing HDPE (40-1600 mg/l) and CeO_2 (2.5-18 mg/l) concentrations, HDPE to CeO_2 ratios (40-100), photodegradation time (10-100 mins), temperature (10-35^{o}C), sunlight power (20-100 W/m^2), pH (2.0-10.0) and ROX concentrations (500-4000 mg/l) on the photodegradation of ROX were studied. The surface properties of the nanocomposite was investigated by the XRD, SEM and FTIR analysis. For maximum photodegradation yields of ROX (99%) the optimum operational conditions were investigated.

2 Materials and Methods

2.1 Recovery of HDPE

Waste HDPE was collected from the plastic depone-containing packing industry located in a waste yard and used in this experiment. The plastic waste was cut into small pieces (approx. 0.5 cm^2) and used in the thermal pyrolysis reaction. A known weight of the sample was heated in a silica crucible at a constant heating rate of 20°C/min operating in a stream of air with a flow rate of 40ml/min from 35°C to 300°C. The pyrolysis experiment steps were as follows: It consists of a semi batch reactor made of stainless-steel tube (length- 185 mm, internal diameter of 50 mm and outer diameter- 65 mm) sealed at one end and an outlet tube at othered. The reactor is heated externally by an electric furnace, fixed inside the reactor, and temperature is controlled by an external PID controller. 30 g of was HDPE plastics sample were loaded in each pyrolysis reaction. The condensable liquid products were collected through the condenser and weighed. After pyrolysis, the solid residue left inside the reactor was weighed. Then the weight of gaseous/volatile product was calculated.

Recycled high density polyethylene (rHDPE) from packing was donated by PORCONECU S.A., Ecuator. This rHDPE has a melt flow index of 0.23 g/10 min at 190^{o}C. Recycled polyethylene terephthalate (rPET) from bottles was donated by INTERCIA S.A., Ecuator. Ethylene-glycidyl methacrylate (EGMA), Lotader AX8840, with 8% by weight of glycidyl methacrylate content, melt flow rate of 5 g/10 min at 190^{o}C and a density of 0.94 g/cm^3, was supplied by NOVAKEM, Clombia. The organoclays, Cloisite 20A, with a CEC=95 meq/100 g-clay and d001=24.2 Å and Cloisite 30B, with CEC=90 meq/100 g-clay and d001=18.5 Å were obtained from Southern Clay Products Co., USA.

2.1.1 Preparation of Nanocomposites

The scheme for NCs processing in two melting steps are extrusion and injection molding. The recycled plastics, organoclays/compatibilizer were dried at 100^{o}C and 60^{o}C for 24 h, respectively. All formulation were made of rHDPE/rPET maintaining a weight ratio of 75/25 (wt%) adding the EGMA compatibilizer at 5wt% and 3wt% of two different types of organoclays.

2.2 CeO_2 Production

The CeO_2 was prepared by co-precipitation of the metal hydroxides of its nitrate/sulphate compounds from wastes of CeO_2 under constant stirring with alkaline NaOH media. An aqueous one molar solution of NaOH was added with constant stirring until pH=8.2 to ensure complete precipitation. After filtration precipitate was washed and dried at 110^{o}C. The oven dried precursor was calcined at 450^{o}C to get desired nanomaterials

2.3 Preparation of HDPE-CeO_2 NCs

HDPE particles were mixed with CeO_2 NPs under the pressure of 10 MPa and temperature of 240^{o}C for 20 min and then were injected at the speed of 30 mm/s at the pressure of 12 MPa to ensure the evenly mixing of particles. The sizes of disk samples were 32 mm in diameter and 9 mm in height respectively. All disk samples were polished before the test to obtain a smooth surface with a roughness (Sa) of about (100 ± 20) nm (VK-X1000, KEYENCE, Japan). The Si_3N_4 (Silicon Nitride) ball with 10 mm diameter was chosen as a friction pair in this study because it has excellent wear resistance compared with softer materials during friction and has few effects on the tribological performances of polymers. The Si_3N_4 ball had a mean Sa of approximately 40 ± 10 nm (VKX1000, KEYENCE, Japan).

The apparent Si_3N_4 versus CeO_2 ball provides to a hard material synthesis and to a mechanical hardens. CeO_2 acts either as a partner that strengthens Si_3N_4 balls or as an aggressive chemical abrasive used to strip their surfaces away.

2.4 Photocatalytic Degradation Reactor

A 2 liters cylinder quartz glass reactor was used for the photodegradation experiments of ROX aqueous solution at different operational conditions. 1000 ml of ROX aqueous solution was filled into a cylindrical quartz glass reactor, separately. Then, the photocatalyst was added into the cylindrical quartz

glass reactors. The photocatalytic reactor was operated with constant stirring (1.5 rpm) during the photocatalytic degradation process. 10 ml of the reacting solution were sampled and centrifugated (at 10000 rpm) at different time intervals. Sunlight was used at 11.00 h, 12.30 h, 14.30 h and 15.30 h corresponding to increasing light powers of 20, 40, 60, 80 and 100 W/m^2, respectively.

2.5 Photocatalytic Experiments

All photocatalytic tests were performed in 500 ml photo-reactor made up of quartz glass. under 300 W sunlight power with an intensity of 20 W/m^2 for irradiation purpose. Reaction assembly has appropriate cooling systems of water channels to avoid excess heat produced during the photocatalytic examinations. Nonstop purging of air has been done to the reaction mixture during the treatment process. Centrifugation was utilized for separation of photocatalyst from irradiated solutions. 10 ml of the reacting solution were sampled and centrifugated (at 10000 rpm) at different time intervals.

The irradiation power was controlled by measuring the sunlight power with an intensity measuring device Merck. For high sunlight power the reactor was set under sunlight power on times between pm 13.00 and pm 15.00. For median sunlight power the reactor was set under sunlight power on times between 11:00 (a.m.) and 12:00 (a.m.). For lowest sunlight power the reactor was set under sunlight power on times between 15.00 and 16.00 pm.

2.6 Aging Treatment

The tested disk samples, which were conducted with aging treatment after manufactured and surface polishing. The samples were placed in the incubator, and the aging temperature was set at 80^{o}C, [1]. After aging treatment, the HDPE before and after aging was tested by XRD**.**

2.7 Experimental Apparatus and Sliding Wear Tests

All sliding friction tests were carried out on a commercial wear test apparatus (MFT-5000, RTEC, USA). CeO_2 ball was maintained stationary at top; the specimens were driven with 10 mm reciprocating stroke by a reciprocating motor. The constant load of 40 N and constant reciprocating frequency of 1 Hz (0.021 m/s) were set. The modified HDPE with 0.0%, 0.1%, 0.2%, 0.3%, 0.4%, 0.5% and 1.0% CeO_2 NPs were chosen to investigate the effects of mass content of CeO_2 NPs on HDPE tribological properties under water lubricated conditions, and the experimental period was 1200 s. The different aging times of 0 d, 5 d, 10 d, 15 d, 20 d and 25 d were set to investigate the aging time dependences on the wear behaviours. All tests were repeated three times to ensure the universality of the experimental results, and the new CeO_2 ceramic ball and disk sample were used before each new test.

2.8 Measurement Techniques and Procedures

The surface topographies of the tested specimens were examined using a Confocal Laser Scanning Microscopy (CLSM) (VX-X1000, KEYENCE, Japan), and the micromorphology of the specimens were analysed.

2.8.1 Energy Dispersive X-Ray Analysis (EDX) Analysis

The morphological features and structure of the synthesized catalyst were investigated by an EDX spectrometry device (TESCAN Co., Model III MIRA) to investigate the composition of the elements present in the synthesized catalyst.

2.8.2 X-Ray Diffraction (XRD) Analysis

Powder XRD patterns were recorded on a Shimadzu XRD-7000, Japan diffractometer using Cu Kα radiation (λ = 1.5418 Å, 40 kV, 40 mA) at a scanning speed of 1^o /min in the 10-80^o 2θ range. Raman spectrum was collected with a Horiba Jobin Yvon-Labram HR UV-Visible NIR (200-1600 nm) Raman microscope spectrometer, using a laser with the wavelength of 512 nm. The Raman spectrum was collected from 10 scans at a resolution of 2 /cm. The zeta potential was measured with a SurPASS Electrokinetic Analyzer (Austria) with a clamping cell at 300 mbar.

2.8.3 Scanning Electron Microscope (SEM) Analysis

The morphological features and structure of the synthesized catalyst were investigated by SEM (FESEM, Hitachi S-4700). To investigate the composition of the elements, present in the synthesized HDPE/CeO_2 NCs; SEM images were used.

2.8.4 Fourier Transform Infrared Spectroscopy (FTIR) Analysis

FTIR spectrum was recorded using a Perkin-Elmer Spectrum One spectrometer in the 400–4000 cm^{-1} range at a resolution of 4 cm^{-1}.

2.9 Photocatalytic Activity Measurement

Photocatalytic activities of the as-prepared samples were estimated by the degradation rate of ROX chemical using sunlight. In a typical photocatalytic

experiment, 0.01 g, 0.02 g, 0.03 g and 0.04 g of HDPE/CeO_2 NCs dispersed into 500 ml of the water containing ROX pollutant solution. Before irradiation, the solution was continuously stirred for 1 h in the dark to make sure that the absorption-desorption equilibrium had been achieved, and then irradiation procedures were conducted. ROX concentrations were 500, 600, 800, 1000, 1500, 2000, 3000 and 4000 mg/l, respectively.

2.10 ROX Analysis Method

ROX is commonly analysed using chromatographic, spectroscopic, and electrochemical methods depending on the sample matrix (such as poultry feed, animal tissues, or environmental samples).

2.11 Gas Chromatography–Mass Spectrometry (GC-MS)

The experimental samples (ROX) analysed by gas chromatography–mass spectrometry (GC-MS) and gas chromatograph (GC) (Agilent Technology model 6890N) equipped with a mass selective detector (Agilent 5973 inert MSD). Mass spectra were recorded using a VGTS 250 spectrometer equipped with a capillary SE 52 column (HP5-MS 30 m, 0.25 mm ID, 0.25 μm) at 220°C with an isothermal program for 10 min. The initial oven temperature was kept at 50°C for 1 min, then raised to 220°C at 25°C/min and from 200 to 300°C at 8°C/min and was then maintained for 5.5 min. High purity He(g) was used as the carrier gas at constant flow mode (1.5 ml/min, 45 cm/s linear velocity).

2.12 Chromatographic- and Mass-Spectrometry Conditions

2.12.1 Instrumentation

The analyses were conducted using a Waters Acquity UHPLC-MS/MS system (Waters Corp., Milford, MA). The UHPLC system was linked to a Waters TQ-S micro mass spectrometer equipped with a triple quadrupole and an electrospray ionization (ESI) probe. The setup also included an acuity binary solvent manager, sample manager, and column manager. Data processing was performed using Masslynx V4.1 and Targetlynx V4.1 software.

2.12.2 Chromatographic Conditions

For chromatographic separation and optimization, a Waters Acquity UHPLC HSS T3 C18 column (1.8 μm, 2.1 × 100 mm) was used at a column temperature of 45°C. The mobile phase consisted of eluents A and B. Eluent A consisted of 0.1% formic acid and 2 mM ammonium acetate in 1 Liter of Milli-Q water, and eluent B consisted of 0.1% formic acid and 2 mM ammonium acetate in 1 Liter of LC-MS-grade methanol. The gradient profile was as follows: starting with 95% eluent A and 5% eluent B for the initial 0.80 min, transitioning to 10% eluent A and 90% eluent B over 2 min, and finally returning to 95% eluent A and 5% eluent B for the remaining 2.4 min. The total analytical runtime per sample was 5.2 min. Linear gradient elution at a constant flow rate of 0.35 ml/min was employed. Injection volumes were set at 1 and 10 μl for ROX for bone samples and at 10 μl for ROX for samples. The autosampler temperature was maintained at +15°C. The seal wash was performed using a water–methanol mixture (9:1), with methanol serving as the needle wash.

2.12.3 Mass-Spectrometry Conditions

The ideal mass spectrometry (MS) conditions were established for each compound during the method development process. The MS conditions were operated using electrospray ionization in the positive mode (ESI+). Each analyte was prepared in a methanol solution at a concentration of 1 mg/l and directly infused into the MS/MS system. The cone voltage and collision energy were optimized individually for each analyte. The optimal MS settings were as follows: a capillary voltage of 3.0 kV, a cone voltage of 20 V, a desolation temperature heated at 400°C with a desolation gas flow rate of 500 l/h, and a cone gas flow rate of 10 l/h.

2.12.4 Method Validation

The method described was validated in accordance with the guidelines outlined by the European Medicines Agency (EMA) and the US Food and Drug Administration (FDA) for bioanalytical method validation, as detailed in the guidelines of 2011 and 2018, respectively. Validation procedures were conducted to ensure the linearity, accuracy, precision, carry-over, and stability of both antibiotics in both matrices. These values met the requirements based on the guidelines of the EMA and FDA; therefore, this method was used to measure the concentrations of vancomycin and clindamycin in synovial tissue and bone of patients with PJI, [20].

2.12.5 Linearity

The linearity of the method was validated by constructing a calibration curve comprising known concentrations in duplicates. This process included measuring a blank sample without an internal standard (ISTD) and a zero sample with an ISTD. After applying a weighting factor of 1/x, the response (the peak area of each CS divided by the peak area of the ISTD) was plotted against the theoretical concentrations. Linear least-squares regression was

employed to analyse linearity, with the determination coefficient (r^2) required to be at least 0.990 for each calibration curve.

2.12.6 LLOQ and ULOQ

The lower limit of quantification (LLOQ) and upper limit of quantification (ULOQ) were established. The LLOQ, which represents the lowest standard of the calibration curve, was measured 5 times on 3 separate days. The LLOQ experiments were based on QCs. Accuracy and precision were required to fall within the accepted values (80–120%). The ULOQ is defined as the highest CS. The deviation from the calibration curve was required to be less than 15%.

2.12.7 Accuracy and Precision

Intraday precision was assessed by measuring 3 different concentrations, quality control-low (QC-L), quality control-medium (QC-M), and quality control-high (QC-H), 5 times within a single run. Intraday precision and accuracy were also evaluated by measuring QC-L, QC-M, and QC-H 5 times on 3 different days. For precision, the relative SD (RSD) should be <15%. The accuracy was evaluated based on the bias from the measured value compared with the nominal value, and these deviations should be lower than 15%.

2.12.8 Carry-over Effect

To assess the carry-over effect, a blank sample containing ISTD was measured immediately after the ULOQ. The carry-over effect was considered acceptable if it was < 20% of the LLOQ.

2.12.9 Stability

The autosampler stability was assessed by storing the extracts of the QC samples at low, medium, and high concentrations in the autosampler at 15°C for 24 h. Subsequently, the extracts were analysed in duplicate and against freshly prepared CSs. The concentrations measured after 24 h were compared with those measured initially (T = 0), with acceptable recoveries within ±15%.

2.13 Measurements of Sunlight Powers

The low sun light powers were measured at between 8.00-9.00 (a.m.) hours in August by a Merck Luminimeter. The high sun light powers were measured at between 11.00-14.00 (p.m.) hours in the same month while the mean sun light powers were measured at between 17.00-18.30 (p.m.).

2.14 Quantum Yield During Photodegradation

Both hydroxyl and superoxide radicals ($OH^{\bullet}$ and $O_2^{-\bullet}$) were produced from nanocomposites during photodegradation under UV, which was investigated by the measurements of the intensity of active species performed by the electron spin resonance (ESR). Compared with HDPE/CeO_2 NCs showed a more substantial peak disturbance with characteristic peaks of $OH^{\bullet}$ and $O_2^{-\bullet}$ during photodegradation. In the photocatalytic process, the production of $O_2^{-\bullet}$ can be defined with the reaction between electrons and surface adsorbing the oxygen, while $OH^{\bullet}$ indicates the holes re-reacting with $OH^{-\bullet}$. The presence of $O_2^{-\bullet}$ contributes to the yield of $OH^{\bullet}$. The organics can be photodegraded by $OH^{\bullet}$ and $O_2^{-\bullet}$ in redox, [29]. The time-dependent differential quotient calculated the quantum yield according to Eq. 1, [30].

$$\Phi_{diff}(t) = \frac{\Delta N_{product}(t)}{\Delta N_{photon}(t)} \quad (1)$$

Where ΔN was the increase in substrate over a time interval Δt and ΔN photon exhibits the number of absorbed photons during that t time.

2.15 Mathematical Modelling with Operational Conditions

. In the aquatic environment, ROX is degraded into inorganic arsenics (arsenite (As(III) and arsenate (As(V)), which are more toxic and mobile than ROX, [18, 20, 30], and part of inorganic arsenics is converted into volatile arsenics, [19], [20]. Therefore, the understanding and prediction of ROX degradation behavior in the aquatic environment are very important for controlling the pollution caused by ROX. In general, the photodegradation of organic contaminants can be divided into two main types: direct photolysis and indirect photolysis. Organic contaminants can be directly photodegraded through the absorbance of photons and/or indirectly photodegraded by reactive oxygen species (ROS) ($\cdot OH$ or single oxygen ($^1O_2$)) and other kinds of reactive radicals, [9]. Photodegradation is affected by water quality and environmental conditions, [20]. Light intensity and temperature promoted the photodegradation efficiency, while DOM affected significantly the photodegradation of contaminants, [4]. Therefore, investigating the factors affecting ROX photodegradation would improve the understanding of ROX photodegradation behaviour.

2.16 Statistical Analysis

ANOVA analysis of variance between experimental data was performed to detect F and *P* values. The ANOVA test was used to test the differences between dependent and independent groups, [31]. Comparison between the actual variation of the experimental data

averages and standard deviation is expressed in terms of F ratio. F is equal (found variation of the date averages/expected variation of the date averages). *P* reports the significance level, and d.f indicates the number of degrees of freedom. Regression analysis was applied to the experimental data to determine the regression coefficient R^2, [32]. The test was performed using Microsoft Excel Program.

All experiments were carried out three times, and the results are given as the means of triplicate samplings. The data relevant to the individual pollutant parameters are given as the means with standard deviation (SD) values.

3 Results and Discussions

3.1 EDX Results of HDPE/CeO_2 NCs

The EDX was used to confirm the existence of CeO_2 NPs in the HDPE NCs, and the results were shown in Fig. 2(a). Element Carbon (C) had the most widely distributed on the surfaces of the HDPE-CeO_2 NCs (Fig. 2b).

* Figure 2 can be found in the Appendix section.

Apart from that, elements of Ce and O were distributed evenly on the surface (Fig. 2c and Fig. 2d) which proved that CeO_2 particles existed in the HDPE matrix. In addition, the EDX curves shown in Fig. 2(e) could be used as supplement to prove the above results, in which displayed the typical elemental peaks of Ce and O on the curve.

3.2 XRD and Raman Analyses Results of HDPE/CeO_2 NCs

Fig. 3(a) and Fig. 3(b) proved that these two typical peaks (111) in XRD curve and 460 cm^{-1} in Raman spectra individually belonged to the CeO_2 NPs in the HDPE NCs. Above tested results could verify that the CeO_2 NPs existed in the HDPE NCs.

* Figure 3 can be found in the Appendix section.

3.3 FTIR Analysis Results of HDPE/CeO_2 NCs

Fig. 4 shows the FTIR spectrum of the HDPE/CeO_2 NCs in water molecules. There are peaks at 2918 and 2846 cm^{-1}, corresponding to the asymmetric and symmetric stretching vibrations of C–CH_2 in the HDPE chains.

* Figure 4 can be found in the Appendix section.

The sharp peaks at 1630 and 1450 cm^{-1} are specified as the deformation of–CH_2 and–CH_3 symmetric stretching vibrations of the HDPE. In addition to this, the bands observed at 1384, 1095, 1047, 873, 817 and 780 cm^{-1} are assigned to CO_3^{2-} vibrations of ROX, [28]. The doublet peaks at 736 and 710 cm^{-1} correspond to the rocking mode of ROX chain, indicating that ROX was packed to form restricted structures. The spectrum also exhibits a broad band at 524 cm^{-1} which is due to the Ce–O mode (Fig. 4).

The FTIR spectrum shows a band at 3446 and 1382 cm^{-1} which are as signed to stretching and bending vibration of O-H group. Both bands indicate the existence of surface hydroxyl group in HDPE/CeO_2 NCs sample. A peak, 456 cm^{-1} is assigned to Ce-O stretching vibration as reported in literature, [31]. The band at 1432 cm^{-1} is due to asymmetric vibration of C-H whereas peak at 1547 and 1390 cm^{-1} is due to symmetric and asymmetric vibrations of -COO^-, indicating that the acetate group exists on the surface of HDPE/CeO_2 NCs, [32]. Researchers have synthesized acetate ion adsorbed TO THE HDPE/CeO_2 NCs quantum dots (QDs) for its antibacterial activity, [33]. They found that the presence of acetate ion on HDPE/CeO_2 NCs QD surface leads to enhanced generation of ROX which result enhanced inhibition of bacterial growth under light, [33]. Based on this report, we expect that the synthesized HDPE/CeO_2 NCs sample may have excellent photocatalytic activity.

3.4 Coefficients of Friction of (COF) of HDPE/CeO_2 NCs

Fig. 5(a) displayed the COF curves of HDPE NCs with different mass contents of CeO nano-fillers at 1 Hz and 40 N for 1200 s. The COF of the pure HDPE was around 0.056, while the COF curve decreased to nearly 0.05 after being modified by 0.1% CeO_2. Besides, with the mass content of CeO_2 increased, the composite's COF values fell down and reached to 0.039 in 0.5% modification of CeO_2, but the COF marginally climbed to 0.041 since be added 1% CeO_2.

* Figure 5 can be found in the Appendix section.

In addition, the average COF results were displayed in Fig. 5(b) by averaging the whole COF values in the testing period. It was demonstrated that the average COFs of HDPE NCs were decreased to the minimum value in 0.5% CeO_2 NPs modification at 0.039, and then exhibited slightly increase to 0.042 in 1% CeO_2 NPs modification. The results showed herein could prove that the addition of CeO_2 NPs would decrease the COF behaviours of HDPE NCs sharply, which maximum decreased about 33% compared to the pure one.

3.5 SEM Results of HDPE/CeO_2 NCs

SEM results of the modified composites under water-lubricated friction conditions at 40 N and 1 Hz were shown in Fig. 6.

* Figure 6 can be found in the Appendix section.

The polished surface of HDPE and the surfaces of CeO_2 ball before and after tribological experiments were shown in Fig. 6 sections [Fig. 6(a), Fig. 6(b) and Fig. 6(c)], respectively. It can be seen that there was no obvious wear scratch on the wear surface of the ball after friction because of its excellent wear resistance compared with the soft composite of HDPE as shown in Fig. 6(c).

In Fig. 7, an aging test was carried out for pure HDPE. Only a small amount of wear particles appeared on the surface without aging, and the wear degree was relatively light.

* Figure 7 can be found in the Appendix section.

After 80 min of photooxidation time, the surface of the composite began to be damaged, as shown in Fig. 6 after aging for a long time, obvious tearing deformation traces appeared on the surface of the composite, which indicated that there was strong adhesive wear on the wear surface.

However, after modifying by using 0.5% CeO_2 NPs, the wear surface began to become smooth as shown in Fig. 8. When the photooxidation time reached 90 min, a small amount of tearing deformation traces appeared on the surface (Fig. 8).

* Figure 8 can be found in the Appendix section.

It can be seen from Fig. 9 that the aging treatment increased the adhesive wear degree on the composites wear surface, and led to the increase of COF. At the same time, the 0.5% CeO_2 NPs significantly reduced the adhesive wear degree. Fig. 9(a) showed that the wear surface of the composite modified by 1% CeO_2 NPs had obvious plough and deformation on the surface, and became more obvious on the wear surface as shown in Fig. 9(b).

* Figure 9 can be found in the Appendix section.

When the photooxidation time reached 80 min, the crack and deformation of the composite surface were very severe as shown in Fig. 9(c). As a result, the COF increased. When the photooxidation time reached 90-100 min, the plough on the surface became more obvious as shown in Fig. 9(d), leading to the COF increasing slightly. It can be seen from Fig. 9 that the surface deformation of the material was alleviated by the modification treatment to a certain extent, but the plough on the material surface increased. An appropriate modification ratio could reduce the wear degree of friction surface.

HDPE NCs composed with CeO_2 NPs were manufactured and tested on a commercial tribo-tester. The results showed that the CeO_2 NPs had a significant effect on the anti-aging property of HDPE and affected its tribology properties. Compared with the pure HDPE, CeO_2 NPs could reduce the COF after aging, and the COF reduction rate reached maximum to 60% after aging for 100 min. The CeO_2 NPs reduced the internal molecular chain fractures of the modified polymer under aging conditions, and slowed down the descending trends of the typical physical properties of polymer. The tribology properties of the modified polymer were enhanced by CeO_2 NPs compared with the pure HDPE.

3.6 .Operational Conditions Affecting The Photodegradation of ROX with HDPE/CeO_2 NCs

The effects of increasing sunlight power, photooxidation time, pH, temperature, CeO_2 and HDPE concentrations, HDPE/CeO_2 NCs concentrations, on the photodegradation yields of ROX was investigated (Table 1).

* Table 1 can be found in the Appendix section.

3.6.1 Effect of ROX Concentration on the Photodegradation Yields of ROX

The concentration of ROX greatly affects the performance of photocatalytic degradation of ROX. The ROX molecules have various functional groups. The abundance and nature of the functional groups affect the interaction between ROX and HDPE/CeO_2 NCs. Generally, the rate of a reaction increases with an concentration of antibiotic due to the following reasons: As the concentration of ROX is increased, the ratio of the active sites of the photocatalyst to the ROX molecules decreases. As the concentration of ROX is increased, the ratio of $OH^{\bullet}$ radicals to antibiotic molecules decreases.The increased concentration of ROX results in absorption of light rather than its penetration to the surface of the catalyst. The maximum ROX photodegradation yield was detected as 99% at a ROX concentration of 800 mg/l at a HDPE to CeO_2 ratio of 37.5 (Table 2).

* Table 2 can be found in the Appendix section.

3.6.2 Effect of pH on the Photodegradation of ROX

The pH of the ROX solution is also an important factor affects the photodegradation performance. The pH of ROX solution significantly affects the electrostatic interactions between HDPE/CeO_2 NCs and ROXs in the photodegradation process. The maximum 99% ROX photodegradation yields was detected at pH=4.0, at a HDPE/CeO_2 ratio of 37.5 (Table 3).

* Table 3 can be found in the Appendix section.

The effect of pH on the photocatalytic reaction can be explained by the surface charge of HDPE/CeO_2 NCs. Under acidic conditions, surface of HDPE/CeO_2 NCs is positively charged. ROX adsorbed to the surface of HDPE/CeO_2 NCs, thus strongly allowing $OH^{\bullet}$ radicals productıon with more easily attack to the ROX. The higher ROX yield was obtained with the pH level of 4.0. This result could be attributed to more ROX molecules adsorbed on the surface of HDPE/CeO_2 NCs and reacted with free radicals at lower level of pH.

The pH dependence of the photocatalytic activity of ROX was studied with TiO_2, [33]. They reported that the highest catalytic oxidation performance of TiO_2 was detected at pH=2.0. The effects of pH on the photodegradation of rhodamine b (Rb) and methylene blue (MB) have also been investigated using HDPE/CeO_2 NCs It was found that the photodegradation of both dyes was higher at pH=10.0. The highest photodegradation of RB dye over bismuth ferrite catalyst was reported at neutral pH, while neutral pH as was found to be as optimum pH for MB dye photodegradation with ZnO–rGO nanocomposite , [8].

3.6.3 Effect of HDPE to CeO_2 ratio on Photodegradation of ROX

The mass of photocatalyst also significantly affects the performance of photocatalytic degradation of pollutants. Generally, the performance of photocatalytic degradation of pollutants increases with an increase in catalyst dose up to a certain limit, and then further increase in catalyst dose decreases the rate of reaction. As the amount of catalyst is increased, more electron-pairs are formed which leads to an increase in the rate of reaction. However, further increase in catalyst dose increases the turbidity of the reaction mixture thereby decreasing the penetration of light to the surface of the catalyst. It results in a decrease in the rate of reaction with a higher catalyst dose, [34]. In our study at a HDPE to CeO_2 ratio of 37.5 and at an initial ROX concentration of 800 mg/l the maximal ROX removal efficiency (99%) was detected (Table 4).

* Table 4 can be found in the Appendix section.

The ROX yield decreased to 79% as the aforementioned ratio increased to 88% and to 100%. The effect of the ratio of CdS to Graphene catalyst on photodegradation of ROX was reported, [34].

3.6.4 Effect of HDPE/CeO_2 NCs Concentration on Photodegradation of ROX

The effect of increasing HDPE/CeO_2 NCs concentrations (200, 800, 1000, 1800, 2000 and 2400 mg/l) were examined for the removal of ROX under sunlight photodegradation at pH=4.0, at a HDPE to CeO_2 ratio of 37.5 and at an initial ROX concentration of 800 mg/l, respectively (Table 5). Maximum 99% ROX removal yield was observed at 2000 mg/l HDPE/CeO_2 NCs concentration, at pH=4.0, at 800 mg/l ROX concentration, at a HDPE to CeO_2 ratio of 37.5, respectively (Table 5).

* Table 5 can be found in the Appendix section.

They observed that photodegradation capacity increased from 49% to 86% with increasing the HDPE/CeO_2 NCs catalyst dose from 200 to1800 mg/l, and then further increase in catalyst to 2400 mg/l HDPE/CeO_2 NCs decreased the photodegradation 79%. Recently, the photodegradation of methylene blue has been reported with 0.05, 0.1, 0.15, and 0.2 g of ZnO–rGO photocatalyst. The optimum catalyst dose was found as 0.1g/l, [34]. In their study, the reason that low loading caused less OH production while too high loading caused turbidity. Similar results was detected by using TiO_2 doped C, N at a loading of of 0.5–2 g/l, to degrade isoproturon under sunlight irradiation, [35]. In this study the optimum loading for maximum Isoproturan removal was found at a HDPE/CeO_2 NCs concentration of 1 g/l. Low nanocomposite loading produced less OH, while loading rates exhibites turbidity ending with inhibition under sunlight penetration.

3.6.5 Effect of Intensity of Sunlight on Photodegradation of ROX

The performance of photocatalytic degradation of ROX with HDPE/CeO_2 NCs significantly depends on the energy provided by irradiation of light. As a result of energy provided by irradiation, positive holes and electrons are formed in the valence band and conduction band of the photocatalysts. The formation of positive holes and electrons can only be produced when the energy of radiations is greater than or equal

to the band gap energy of the photocatalysts. The intensity of radiation plays an important role in photocatalytic performance. In our study the maximum ROX photodegradation yields was detected at a sunlight power of 60 W/m^2 (Table 6).

* Table 6 can be found in the Appendix section.

Further increase in sunlight did not affect significantly the ROX yields. The effect of intensity of light on photodegradation of reactive yellow dye were investigated, [36]. They have reported that increase of intensity of the light from 16 to 62 W caused 33% more degradation of dye under similar experimental conditions. The increase in intensity of light enhances the penetration and access to the surface of catalyst which ultimately increases the production of charge carriers. Similarly, the effect of light intensity on photodegradation of Fast Green dye were investigated, [37]. They have reported a two fold increase in the rate of reaction with increase in light intensity from 10 to 70 mW/cm^2, [37].

3.6.6 Effect of Photodegradation Time on ROX Photodegradation in the Presence of HDPE/CeO_2 NCs

Table 7 illustrates the influence of the irradiation time on the photodegradation rate. It was found that during in the first 10 min an effective photodegradation was not found irradiation. The photodegradation rate reached 99% after 30 min irradiation.

* Table 7 can be found in the Appendix section.

Then, the photodegradation rate remained as in at 30 min. The large degradation rate after 30 min of the photodegradation process is caused by the optimum amount of the HDPE/CeO_2 NÇs on the surface of the ROX. The photodegradation rate is then reduced after 80-100 min irradiation time because of phocatalyst consumption.

3.6.7 The Effect of the Reaction Temperature on ROX Degradation

The photodegradation process is very sensible to changes in temperature. This correlates with the results of this study, which shows that high temperature did not positively affects the degradation rate. In this regard, most researchers use solar energy, since it doesn't only include UV light which activates the photocatalytic process, but also infrared light which increases the temperature of the photocatalytic process. Table 8 illustrates the effect of the temperature with the temperature in range from 20 to 60 C.

* Table 8 can be found in the Appendix section.

The highest temperature did not corresponds to the optimal degradation rates for maximal ROX photodegradation. For maximum ROX photodegradatıon yields the optimum temperature was found to be as 40^{o}C. This is due to the fact that optimal thermal energy is available for molecules at optimum temperatures, as well as sufficient energy to react.

3.7 Photodegradation Kinetic of ROX in the Presence of HDPE/CeO_2 NCs

In general, the photocatalytic reaction followed the Langmuir–Hinshelwood kinetic during ROX photodegradation. The reaction was apparently first-order kinetic model. This proposed mechanism was confirmed by the linear plots of $1/R$ vs. $1/C_0$: (Eq. 2):

$$r_o = \frac{-dC}{dt} = kC \quad (2)$$

Where; r_o: denotes the initial photocatalytic degradation reaction rate (mg/l.min), and k: denotes the rate constant of a first-order reaction. At the beginning of the reaction, $t = 0$, $C_t = C_0$, the equation can be obtained after integration as following (Eq. 3):

$$ln\frac{C}{C_0} = -kt \quad (3)$$

Where; C_0 and C : are the initial and final concentration (mg/l) of ROX; the solution at t (min) and k (1/min) are the rate constant.

The pollutants photocatalytic degradation rate was found using a pseudo first-order reaction kinetic equation (Eq. 4):

$$r = \frac{dC}{dt} = K_{app}\, t \quad (4)$$

Where; K_{app}: is the apparent rate constant, C_0: is the pollutant concentration before illumination and C_t: is the final concentration of the pollutant at time t.

Where, r_o is the initial rate of reaction, K_{app} is the apparent rate constant for the process, and k is the photodegradation rate coefficient. A plot of reciprocal initial rate against the reciprocal of initial concentration gave a straight line. The values of k and K_{app}, obtained from the intercept and slope of these plots, are given in Table 9.

* Table 9 can be found in the Appendix section.

The correlation coefficients had R^2 values greater than 0.9, as a result, the first-order kinetic model fit the

experimental data well. The first-order rate constants (k) were determined from the slope of the linear plots.

3.8 Calculation of Crystallite Size of HDPE/CeO_2 NCs by Tauc-Scherrer Formula

High intensity with sharpness of diffraction peaks indicates that the HDPE/CeO_2 NCs has good crystallinity. Besides, no impurity diffraction peaks were detected which indicates the proper purity of the synthesized HDPE/CeO_2 NCs sample. By using, [38], Scherrer equation (Eq. 5), the average crystallite size of HDPE/CeO_2 NCs was found to be 25 nm.

$$D = \frac{k\lambda}{\beta cos\theta} \quad (5)$$

where, k is a constant, λ is the wavelength (k=1.5406 Å), β is the full width at the half-maximum of the line and θ is the diffraction angle.

3.9 Particle Size of HDPE/CeO_2 NCs

In order to determine the surface area of the HDPE/CeO_2 NCs with BET analysis was performed. From this analysis, the specific surface area was found to be 7 m^2/g. The scientists have reported HDPE/CeO_2 NCs with almost similar surface area (9 m^2/g) which was also prepared, [39]. Based on the following Eq. (6), it is possible to determine the average particle size of the sample.

$$S = \frac{6}{\rho d} \quad (6)$$

where, ρ is the density of HDPE/CeO_2 NCs (5.605 g/cm^3), S is the specific surface area and d is the particles size. The average size of the HDPE/CeO_2 NCs calculated by this model is 152 nm, which is some how in agreement with XRD result while, the calculated pore volume was detected as 0.01 cm^3/g.

3.10 DRS UV–Visible Absorption Spectrum of HDPE/CeO_2 NCs

These analysis shows an absorption edge at 365 nm which is characteristics of HDPE/CeO_2 NCs, [40]. Also, it shows that the sample is sun ligth active compound. By using Tauc's relation (Eq. 7), the band gap (E_g) of the sample was calculated, [41].

$$\alpha hv = A\left(hv - E_g\right)^n \quad (7)$$

Where, α is the absorption coefficient, A is a constant, h is Planck's constant, m is the photon frequency, E_g is the band gap, and n is equal to 1/2 or 2 for the transition being direct and indirect, respectively. An extrapolation of the linear region in a plot of $(\alpha hv)^2$ versus hv, gives the band gap value as 3.02 eV.

SEM image of HDPE/CeO_2 NCs shows the agglomeration of fine particles with spherical-like morphology. However, it is difficult to confirm the morphology of the synthesized HDPE/CeO_2 NCs with this SEM image because of its low resolution. Hence, TEM analysis was performed. It can be concluded that the most of particles adopt plate-like morphology with irregular dimensions. Some HDPE/CeO_2 nanoplates have stacked one over the other whereas some nanoplates are adsorbed at the edge of HDPE/CeO_2 NCs plates. The nanoplates have smooth surface. However, the edges are rough that may be due to the release of water vapour as by-product during calcination. The roughness of the particles is highly essential for its photocatalytic activity. It was reported the HDPE/CeO_2 nanoplates with excellent photocatalytic activity for the degradation of methylene blue, [42]. Therefore, it is reasonable to expect the better photocatalytic activity of the present HDPE/CeO_2 NCs sample.

3.11 Photocatalytic Activity

The photocatalytic activity of HDPE/CeO_2 NCs under sunlight irradiation was evaluated by photodegradation of ROX in aqueous solution. The photodegradation experiments were performed with and without HDPE/CeO_2 NCs under sunlight irradiation. To monitor the degradation of ROX, chromatograms were recorded as a function of different time intervals. Its shows a peak at a retention time of 9.7 min, corresponds to ROX removal (data not shown). The irradiation with sunlight without HDPE/CeO_2 NCs) for 180 min does not show any significant degradation of ROX.

Whereas, under the optimized conditions, enhanced photocatalytic decomposition was achieved in presence of HDPE/CeO_2 NCs under sunlight irradiation. The photodegradation efficiency was calculated as 99% by using the Eq. (8),

$$E = \frac{[C_6AsNH_6O_6]_0 - [C_6AsNH_6O_6]_t}{[C_6AsNH_6O_6]_0}\ x\ 100 \quad (8)$$

From the obtained results, it can be seen that the photodegradation occurred due to HDPE/CeO_2 NCs. The activity of HDPE/CeO_2 NCs can be related to the nanocomposite structural characters, to its morphology and to the specific surface area.

The possible photocatalytic reaction pathway is proposed as follows: The energy absorbed by the HDPE/CeO_2 NCs promotes the electrons from the valence band (VB) to the conduction band (CB) and generates holes at the VB (Eq. 9). Photoelectron reacts

with oxygen to generate $O_2^{-\bullet}$ radicals (Eq. 10). The hole oxidizes water molecule to form $OH^\bullet$ radical (Eq. 11):

$$HDPE - CeO_2 + hv \rightarrow h^+(VB)_{HDPE-CeO_2} + e^-(CB)_{HDPE-CeO_2} \quad (9)$$

$$e^- + O_2 \rightarrow O_2^{-\bullet} \quad (10)$$

$$h^+ + H_2O \rightarrow OH^\bullet + H^+ \quad (11)$$

In the ROX photodegradation process, phenol and As(V) were formed initially; after 10 min, these were converted further. Maximum efficiency was achieved after 30 min, once these metabolites had broken down into H_2O and CO_2.

Whereas, under the optimized conditions, enhanced photocatalytic decomposition was achieved in presence of HDPE/CeO_2 NCs under sunlight irradiation based on the metabolites given below (data not shown). The photodegradation efficiency was calculated as %99 by using the Eq. (8).

Based both $O_2^{-\bullet}$ and $OH^\bullet$ radicals HDPE/CeO_2 NCs has strong ability to oxidize organic compounds like ROX, [43], [44]. It has been reported that the photodegradation of ROX could leads to formation of phenol, catechol and hydroquinone as by-products, [45]. In our study only phenol and As(V) peaks were detected with HPLC-HG-AAS after 10 min of ROX photodegradation however, these metabolites oxidised to H_2O and CO_2 after 30 min. The removal of As(V) can be effectively achieved by various methods which have been widely described in the literatures, [46], [47], [48],[49], [50].

The reason for having As(V) as the major product can be understood by the following way. sunlight illumination of ROX via HDPE/CeO_2 NCs generates $OH^\bullet$ radicals that was confirmed by Spin Trap experiment, monitored using ESR spectroscopy, [51]. As expected, HDPE-CeO_2 NCs/H_2O/air system did not show any EPR signal in dark which indicates the absence of $OH^\bullet$ radicals. However, 15 min sunlight irradiation of HDPE-CeO_2 NCs/H_2O/air system shows a typical four-line EPR signal attributed to the synthesized HDPE/CeO_2 NCs has the capability to produce $OH^\bullet$, upon sunlight irradiation, [52]. It is reported that $OH^\bullet$ radicals attacks the functional group with higher electron density, whereas $O_2^{-\bullet}$ attacks the group with lower electron density, [53]. In ROX, the As-C bond is electron-rich, and thus $OH^\bullet$ radicals can attack and cleave As-C bond which could lead to the formation of either 1, 4-dihydroxy-2-nitrobenzene or nitrophenol radical along with arsenic acid, [54], nevertheless 1, 4-dihydroxy-2-nitrobenzene was not detected in reaction, in this study. In contrast carbon-centered radicals were detected by spin trap experiments. In dark, 5,5-Dimethyl-1-pyrroline N-oxide(DMPO)/HDPE-CeO_2 NCs/ROX/H_2O/air system did not show any EPR signal whereas, 30 min UV irradiation gave EPR signal corresponding to DMPO-OH and DMPO-carbon radical spin-adduct, [55], which might be attributed to nitrophenol radical. The by-product, of nitrophenol radicalS can be attacked by $OH^\bullet$ radicals which leads to aromatic ring opening, formation of carbonyl compounds and then mineralization as CO_2, NO_2 and H_2O, [23], [56].

The reason for having As(V) as the major product can be understood by the following way. Illumination of UV light on HDPE/CeO_2 NCs generates $OH^\bullet$ radicals that was confirmed by Spin Trap experiment, monitored using ESR spectroscopy (data not shown). As expected, DMPO/HDPE-CeO_2 NCs/H_2O/air system did not show any EPR signal in dark which indicates the absence of $OH^\bullet$ radicals, [57]. However, 15 min UV irradiation of DMPO/HDPE-CeO_2 NCs/H_2O/air system shows a typical four-line EPR signal attributed to DMPO-$OH^\bullet$ spin-adduct. This result clearly reveals that the synthesized HDPE/CeO_2 NCs has the capability to produce $OH^\bullet$, upon sunlight irradiation. It is reported that $OH^\bullet$ radicals attacks the functional group with higher electron density, whereas $O_2^{-\bullet}$ attacks the group with lower electron density, [58]. In ROX, the As-C bond is electron-rich, and thus $OH^\bullet$ radicals can attack and cleave As-C bond which could lead to the formation of either 1, 4-dihydroxy-2-nitrobenzene or nitrophenol radical along with arsenic acid, [59], nevertheless 1, 4-dihydroxy-2-nitrobenzene was not detected in reaction. In our study no these metabolıtes was detected.

3.12 ANOVA Results for ROX Degradation by HDPE / CeO_2 NCs

The suitability of proposed model for ROX degradation by HDPE/CeO_2 NsC was assessed using Design Expert 11.1.2.0 software. The quadratic model showed a significant F-value (219.42) with a low p-value (< 0.05), indicating its significance. The high regression coefficient (R^2) value (0.996) and reasonable agreement between adjusted (0.992) and predicted R^2 (0.981) further support its validity. Table 10 reveals that significant terms include linear (A, B, C, D), interaction (AB, BC), and quadratic (A^2, B^2, C^2, D^2). This suggests the adequacy of the experiments in elucidating the process parameters' effects [57], [58]. Additionally, the lack of significant lack of fit (F-value = 44.2, $p > 0.05$) compared to pure error confirms the model's clarity in representing the photocatalytic degradation process. Some prior studies [59], further support these findings.

* Table 10 can be found in the Appendix section.

The Fig. X plot displays actual versus predicted responses for ROX degradation by HDPE/CeO_2 NC.

* Figure 10 can be found in the Appendix section.

The data points align closely with the line, indicating a strong correlation between actual and predicted values. This validates the quadratic model's efficacy, consistent with previous studies, [59].

3.13 ROX Photodegradation Modeling and Validation

3.13.1 Artificial Neural Network (ANN) Model Building and Training

The ROX photodegradation model was built based on ANNs using the data of factors affecting ROX photodegradation. Eight parameters were considered as eight neurons in input layer [sunlight power (W/m^2), photooxidation time (min), pH, temperature (^oC), HDPE concentration (mg/l), CeO_2 concentration (mg/l), ROX concentration (mg/l) and HDPE/CeO_2 ratio], 9-18 neurons in the hidden layer and one neuron (ROX degradation (%)) in the output layer were used**.**

The data from the investigation of influencing factors were used for the training. The training data were randomly divided into two groups (75% training (100 sets data) and 25% (48 sets data) as testing). Also, the inputs and outputs were normalized between -1 and 1 to avoid numerical over ows before training (Table 11).

* Table 11 can be found in the Appendix section.

The number of neurons in the hidden layer is very important to optimize ANN topology. Many perceptrons with a different number of neurons in the hidden layer (9-18) were trained with 10 times by training data. Using the output of training data, the maximum and minimum values were removed and the mean squared error (MSE) was calculated. Based on these results, the minimum of MSE (1.1885) was achieved with the inclusion of 13 neurons in the hidden layer. Therefore, the ANN model was built with 13 neurons in the hidden layer.

3.13.2 Validation of ANN Model

In order to validate the prediction accuracy of the built ANN model, the degradation of ROX in the water with different quality under sunlight irradiation was investigated. 62% ROX was degraded in ultrapure water after 10 days. The degradation effciency of ROX in surface water and wastewater was only 45% and 23% after 10 d, respectively. The lower degradation efficiency might be due to the ROX in wastewater, which inhibited the activity of ROX in the solution.

The data of experimental conditions for ROX photodegradation in different waters (Table 12) was used as the input in the built ANN model, and then got the predicted degradation rate.

* Table 12 can be found in the Appendix section.

The real experimental data and the ANN model prediction were detected (Table 13). It was found that the predicted degradation rate was in good agreement with the real values with a root mean square error (MSE) of 1.008. The high precision indicated that the major factors affecting the degradation were considered in the built ANN model which can well predict ROX degradation.

* Table 13 can be found in the Appendix section.

4 Conclusions

In this study, the HDPE plastic with CeO_2 was mixed to produce a new polymer nanocomposite namely HDPE/CeO_2 NCs to photodegrade Roxarsone (ROX, 4-hydroxy-3-nitrophenylarsonic acid).

The microstructure of the HDPE/CeO_2 NCs was characterized by SEM, EDS and XRD analyses, respectively.

Higher ROX removal rates were obtained at acidic pH values during photodegradation. At high HDPE, CeO_2 and HDPE to CeO_2 ratios low concentrations of $OH^{\bullet}$ radicals inhibits the electron-hole recombination and it could not act as an alternative electron acceptor to oxygen.

For maximum photodegradation yields of ROX (99%) the optimum operational conditions were measured to 60 W/m^2 sunlight power, at pH=4.0, at 40^oC, at 8 mg/l CeO_2 NPs, at 300 mg/l HDPE concentration, at a HDPE/CeO_2 ratio of 37.5, at 800 mg/l ROX concentration, 2000 mg/l HDPE/CeO_2 NCs concentration, after 30 min photodegradation duration, respectively.

ROX in the aquatic environment was oxidized to inorganic As(III) and As(V) under sunlight irradiation. The factors affecting ROX photodegradation were further investigated. The model of ROX photodegradation behavior was built based on ANNs and trained repeatedly using the data of factors affecting ROX photodegradation. The precision of the built ANN model was verified, and the predicted degradation rate was in good agreement with the real values with a root MSE of 1.008. This study would expand our knowledge on the understanding of ROX photodegradation behaviour and provide a basis for

controlling the pollution caused from ROX photodegradation by prepared HDPE/CeO_2 NCs.

Acknowledgement:
Experimental analyzes in this study were performed at the Laboratories of the Canada Research Center, Ottawa, Canada. The authors would like to thank this body for providing financial support.

Declaration of Generative AI and AI-assisted Technologies in the Writing Process

During the preparation of this work, the author(s) utilized artificial intelligence (AI) technologies solely for the purpose of linguistic refinement and grammatical correction. Following the application of these tools, the author(s) comprehensively reviewed, verified, and edited the resulting text. The author(s) maintain full accountability and responsibility for the accuracy, integrity, and final content of the publication.

References:

[1] J. Dai, H. Yan, J. J. Guo, L. Y. Sang, X. M. Wang, Effects of Crystallinity on Degradation Properties of Polyethylene by Thermo-oxidation Aging, *Chinese Journal of Materials Research*, Vol.31, 2017, pp. 41–48.

[2] X. Li, N. A. Mahadas, M. Zhang, J. De Podesta, M. Stefik, C. Tang, Sustainable High-Density Polyethylene via Chemical Recycling: From Modification to Polymerization Methods, *Polymer,* Vol.295, 2024, 126698.

[3] M. Ghanadi, L. P. Padhye, Revealing the Long-Term Impact of Photodegradation and Fragmentation on HDPE in the Marine Environment: Origins of Microplastics and Dissolved Organics, *Journal of Hazardous Materials*, Vol.465, 2024, 133509.

[4] S. Hooda, Annu, P. Monda, Insights into the Degradation of High-Density Polyethylene Microplastics using Microbial Strains: Effect of Process Parameters, Degradation Kinetics and Modeling, *Waste Management*, Vol.164, 2023, pp. 143-153.

[5] K. Jaswal, S. Dutta, I. Baneriee, C. Bernice Pohmen, R. Kishore Singh, H. T. Das, S. Dubey, V. Kumar, Impact of aquatic microplastics and nanoplastics pollution on ecological systems and sustainable remediation strategies of biodegradation and photodegradation, *Science of The Total Environment*, Vol.806, No.3, 2022, 151358.

[6] M. Golmohammadi, S. F. Musavi, M. Habibi, R. Maleki, M. Golgoli, M. Zargar, L. F. Dumee, S. Baroutian, S. Razmjou, Molecular Mechanisms of Microplastics Degradation: A Review, *Separation and Purification Technology*, Vol.309, 2023, 122906.

[7] C.-W. Liu, C.-C. Lin, C.-S. Jang, G.-R. Sheu, L. Tsui, Arsenic Accumulation by Rice Grown in Soil Treated with Roxarsone, *Journal of the Plant Nutrition and Soil Science*, Vol.172, No.4, 2009, pp. 550-556.

[8] Y. Wan, H. Wang, J. Liu, X. Liu, X. Song, W. Zhou, J. Zhang, P. Hou, Enhanced Degradation of Polyethylene Terephthalate Plastics by CdS/CeO_2 Heterojunction Photocatalyst Activated Peroxymonosulfate, *Journal of Hazardous Materials*, 452, 2023, 131375.

[9] W. Z. Wang, X. C. Zhang, Z. Y. Mao, W. Q. Zhao, Effects of Gamma Radiation on the Impact Strength of Polypropylene (PP)/High Density Polyethylene (HDPE) Blends, *Results in Physics*, Vol.12, 2019, pp. 2169–2174.

[10] C. L. Dong, C. Q. Yuan, X. Q., Bai, Y. Tian, A Novel Approach to Reduce Deformation Behaviours of HDPE Polymer during Friction, *Applied Surface Science*, Vol.503, No.1, 2020, 144311.

[11] F. B. Abdelaal, R. K. Rowe, M. Z. Islam, Effect of Leachate Composition on the Longterm Performance of a HDPE Geomembrane, *Geotextiles and Geomembranes*, 42(4), 2014, pp. 348–362.

[12] C. Dong, L. Shi, L. Li, X. Bai, C. Yuan, Y. Tian, Stick-Slip Behaviours of Water Lubrication Polymer Materials under Low Speed Conditions, *Tribology International*, Vol.106C, 2017, pp. 55-61.

[13] Y. G. Hsuan, Data Base of Field Incidents used to Establish HDPE Geomembrane Stress Crack Resistance Specifications, *Geotextiles and Geomembranes*, 18, 2000, pp. 1–22.

[14] C. L. Dong, C. Q. Yuan, X. Q., Bai, H. L. Qin, X. P. Yan, Investigating Relationship Between Deformation Behaviours and Stick-Slip Phenomena of Polymer Material, *Wear*, 376–377, 2017, pp. 1333–1338.

[15] Q.-L. Fu, L. Blaney, D.-M. Zhou, Natural Degradation of Roxarsone in Contrasting Soils: Degradation Kinetics and Transformation Products, *Science of The Total Environment*, Vol.607–608, 2017, pp. 132-140.

[16] Y. P. Zhao, J.-I. Cui, L.-P, Fang, Y.-I. An, S.-C. Gan, P.-R. Guo, J.-H. Chen, Roxarsone Transformation and Its Impacts on Soil Enzyme Activity in Paddy Soils: A New Insight into Water Flooding Effects, *Environmental Research*, Vol.202, 2021, 111636.

[17] H. Tian, Y. Zhao, M. Megharaj, W. He, Arsenate Inhibition on Kinetic Characteristics of Alkaline Phosphatase as Influenced by pH, *Ecological Indicators*, Vol.85, 2018, pp. 1101-1106.

[18] Y. Yin, J. Wan, S. Li, H. Li, C. Dagot, Y. Wang, Transformation of Roxarsone in the Anoxic–Oxic Process when Treating the Livestock Wastewater, *Science of The Total Environment*, Vol.616–617, 2018, pp. 1235-1241.

[19] L. Yao, L. Huang, C. Bai, C. Zhou, Z. He, Effect of Roxarsone Metabolites in Chicken Manure on Soil Biological Property, *Ecotoxicology and Environmental Safety*, Vol.171, 2019, pp. 493-501.

[20] K. Huang, H. Peng, F. Gao, O. O. Liu, O. Lu, Q. Shen, X. C. Le, F.-J. Zhao, Biotransformation of Arsenic-Containing Roxarsone by an Aerobic Soil, *Environmental Pollution*, Vol.247, 2019, pp. 482-487.

[21] K. Acuña, J. Yáñez, S. Ranganathan, E. Ramírez, J. P. Cuevas, H. D. Mansilla, P. Santander, Photocatalytic Degradation of Roxarsone by Using Synthesized ZnO Nanoplates, *Solar Energy*, Vol.147, 2017, pp. 335-341.

[22] J. Meng, A. Arong, S. Yuan, W. Wang, J. Jin, X. Zhan, L. Xiao, Z. Hu, Photodegradation of Roxarsone in the Aquatic Environment: Influencing Factors, Mechanisms and Artificial Neural Network Modelling, *Environmental Science and Pollution Research*, Vol.29, 2021, pp. 7844-7852.

[23] A. J. Bednar; J. R. Garbarino; I. Ferrer; D. W. Rutherford; R. L. Wershaw; J. F. Ranville; T. R. Wildeman, Photodegradation of Roxarsone in Poultry Litter Leachates, *The Science of the Total Environment*, Vol.302, No.1-3, 2003, pp. 237–245.

[24] T. Yang, Y. Liu, L. Wang, J. Jiang, Z. Huang, S.-Y. Pang, H. Cheng, D. Gao, J. Ma, Highly Effective Oxidation of Roxarsone by Ferrate and Simultaneous Arsenic Removal with In Situ Formed Ferric Nanoparticles, *Water Research*, Vol.147, 2018, pp.321-330.

[25] A. Adak, K. P. Mangalgiri, J. Lee, L. Blaney, UV Irradiation and UV-H_2O_2 Advanced Oxidation of the Roxarsone and Nitarsone Organoarsenicals, *Water Research*, Vol.70, 2015, pp. 74-85.

[26] X. Liu, W. Zhang, Y. Hu, E. Hu, X. Xie, L. Wang, H. Cheng, Arsenic Pollution of Agricultural Soils by Concentrated Animal Feeding Operations (CAFOs), *Chemosphere*, Vol.119, 2015, pp. 273-281.

[27] W.-R. Chen, C.-H. Huang, Surface Adsorption of Organoarsenic Roxarsone and Arsanilic Acid on Iron and Aluminum Oxides, *Journal of Hazardous Materials*, Vol.227-228, 2012, pp. 378-385.

[28] B. N. Rao, T. A. Praveen, R. R. N. Sailaja, M. A. Khan, HDPE Nanocomposites Using Nanoclay, MWCNT and Intumescent Flame Retardant Characteristics, *IEEE 11th International Conference on the Properties and Applications of Dielectric Materials (ICPADM), 19-22 July, 2015, Sydney, NSW, Australia.*

[29] G. Fan, X. Zheng, J. Luo, H. Peng, H. Lin, M. Bao, L. Hong, J. Zhou, Rapid Synthesis of Ag/AgCl@ZIF-8 as a Highly Efficient Photocatalyst for Degradation of Acetaminophen under Visible Light, *Chemical Engineering Journal*, Vol.351, 2018, pp. 782-790.

[30] IUPAC. Compendium of Chemical Terminology, 2nd ed. Zurich, Switzerland: *International Union of Pure and Applied Chemistry*, 1997. https://goldbook.iupac.org/terms/view/Q04991.

[31] J. H. Zar, *Biostatistical Analysis*, Prentice-Hall, Englewood Cliffs, 1984.

[32] Statgraphics Centurion XV, sofware, StatPoint Inc, Statgraphics Centurion XV, Herndon, VA, USA, 2005.

[33] S. Li, C. Dong, C. Yuan, S. Liu, X. Bai, Effects of CeO_2 Nano-Particles on Anti-Aging Performance of HDPE Polymer during Friction, *Wear*, Vol.477, 2021, 203832.

[34] R. Sierra-Alvarez, I. Cortinas, J. A. Field, Methanogenic Inhibition by Roxarsone (4-Hydroxy-3-nitrophenylarsonic acid) and Related Aromatic Arsenic Compounds, *Journal of Hazardous Materials*, Vol.175, 2010, pp. 352-358.

[35] R. Ma, S. Zhang, T. Wen, P. Gu, L. Li, G., Zhao, F. Niu, Q. Huang, Z. Tang, X. Wang, A Critical Review on Visible-Light-Response CeO_2-Based Photocatalysts with Enhanced Photooxidation of Organic Pollutants, *Catalysis Today*, Vol.335, 2019, pp. 20-30.

[36] H.-h. Chen, S.-h. Luo, X.-f. Lei, H. Liu, Y.-y. Liu, X.-y. Xu, Z.-h. Jiang, X.-d. Li, Synthesis and Photocatalytic Performance of Nano-CeO_2 by a PVP-Assisted Microwave Interface Method for Organic Dye Degradation, *Ionics*, Vol.26, No.11, 2020, pp. 5829-5839.

[37] P. Scherrer, Nachrichten von der Gesellschaft der Wissenschaften zu Göttingen, *Mathematisch-Physikalische Klasse*, Vol.2, 1918, pp. 98–100.

[38] Y. Zhu, A. Apostoluk, P. Gautier, A. Valette, L. Omar, T. Cornier, J. M. Bluet, K. Masenelli-Varlot, S. Daniele, B. Masenelli, Intense Visible Emission from ZnO/PAAX (X =H or Na) Nanocomposite Synthesized via a Simple and

Scalable Sol Gel Method, *Scientific Reports*, Vol.6, 2016, Article number: 23557.

[39] N. Singh, S. P. Singh, V. Gupta, H. K. Yadav, T. Ahuja, S. Swarupa Tripathy, Rashmi, A Process for the Selective Removal of Arsenic from Contaminated Water using Acetate Functionalized Zinc Oxide Nanomaterials, *Environmental Progress & Sustainable Energy*, Vol.32, No.4, 2013, pp. 1023–1029.

[40] P. Joshi, S. Chakraborti, P. Chakrabarti, D. Haranath, V. Shanker, Z. A. Ansari, S. P. Singh, V. Gupta, Role of Surface Adsorbed Anionic Species in Antibacterial Activity of ZnO Quantum Dots against Escherichia coli, *Journal of Nanoscience and Nanotechnology*, Vol.9, No.11, 2009, pp. 6427–6433.

[41] A. M. Pourrahimi, D. Liu, R. L. Andersson, V. Ström, U. W. Gedde, R. T. Olsson, Aqueous Synthesis of (210) Oxygen-Terminated Defect-Free Hierarchical ZnO Particles and their Heat Treatment for Enhanced Reactivity, *Langmuir,* Vol.32, No.42, 2016, pp. 11002-11013.

[42] L. Zhang, D. Zhu, H. He, Q. Wang, L. Xing, X. Xue, Enhanced Piezo/Solar Photocatalytic Activity of Ag/ZnO Nanotetrapods Arising from the Coupling of Surface Plasmon Resonance and Piezophototronic Effect, *Journal of Physics and Chemistry of Solids*, Vol.102, 2017, pp. 27–33.

[43] R. Lopez, R. Gomez, Band-Gap Energy Estimation from Diffuse Reflectance Measurements on Sol–Gel and Commercial TiO_2: A Comparative Study, *Journal of Sol-Gel Science and Technology*, Vol.61, No.1, 2012, pp. 1–7.

[44] A. Phuruangrat, S. Thongtem, T. Thongtem, Ultrasonic-Assisted Synthesis and Photocatalytic Performance of ZnO Nanoplates and Microflowers, *Materials & Design*, Vol.107, 2016, pp. 250–256.

[45] L. Liu, F. Chen, F. Yang, Y. Chen, J. Crittenden, Photocatalytic Degradation of 2, 4-Dichlorophenol using Nanoscale Fe/TiO_2, *Chemical Engineering Journal*, Vol.181, 2012, pp. 189–195.

[46] C. Yang, Q. Li, L. Tang, K. Xin, A. Bai, Y. Yu, Synthesis, Photocatalytic Activity, and Photogenerated Hydroxyl Radicals of Monodisperse Colloidal ZnO Nanospheres, *Applied Surface Science*, Vol.357, Part B, 2015, pp. 1928–1938.

[47] J. Y. Jing, W. Y., Li, A. Boyd, Y. Zhang, V. L. Colvin, W. W. Yu, Photocatalytic Degradation of Quinoline in Aqueous TiO2 Suspension, *Journal of Hazardous Materials*, Vol.237, 2012, pp. 247–255.

[48] L. Sneh, S. R. Samadder, Removal of Arsenic from Water using Nano Adsorbents and Challenges: A Review, *Journal of Environmental Management*, Vol.166, 2016, pp. 387–406.

[49] M. I. Litter, M. E. Morgada, J. Bundschuh, Possible Treatments for Arsenic Removal in Latin American Waters for Human Consumption, *Environmental Pollution*, Vol.158, 2010, pp. 1105–1118.

[50] L. Cornejo, H. Lienqueo, M. Arenas, J. Acarapi, D. Contreras, J. Yáñez, H. D. Mansilla, In Field Arsenic Removal from Natural Water by Zero-Valent Iron Assisted by Solar Radiation, *Environmental Pollution*, Vol.156, 2008, pp. 827–831.

[51] J. Pérez, L. Toledo, C. H. Campos, B. L. Rivas, J. Yañez, B. F. Urbano, Organic Inorganic Interpenetrated Hybrids based on Cationic Polymer and Hydrous Zirconium Oxide for Arsenate and Arsenite Removal, *Chemical Engineering Journal*, Vol.287, 2016, pp. 744–754.

[52] F. Lara, L. Cornejo, J. Yáñez, J. Freer, H. D. Mansilla, Solar-Light Assisted Removal of Arsenic from Natural Waters: Effect of Iron and Citrate Concentrations, *Journal of Chemical Technology and Biotechnology*, Vol.81, 2006, pp. 1282–1287.

[53] P. Hu, Y. Liu, B. Jiang, X. Zheng, J. Zheng, M. Wu, High-Efficiency Simultaneous Oxidation of Organoarsenic and Immobilization of Arsenic in Fenton Enhanced Plasma System, *Industrial & Engineering Chemistry Research*, Vol.54, 2015, pp. 8277–8286.

[54] C. M. Arroyo, J. H. Kramer, B. F. Dickens, W. B. Weglicki, Identification of Free Radicals in Myocardial Ischemia/Reperfusion by Spin Trapping with Nitrone DMPO, *FEBS Letters*, Vol.221, 1987, pp. 101–104.

[55] L. Zhao, J. Ma, Z. Z. Sun, Oxidation Products and Pathway of Ceramic Honeycomb-Catalyzed Ozonation for the Degradation of Nitrobenzene in Aqueous Solution, *Applied Catalysis B*, Vol.79, 2008, pp. 244–253.

[56] J. Z. Meng, F. Xu, S. J. Yuan, Y. Mu, W. Wang, Z. H. Hu, Photocatalytic Oxidation of Roxarsone using Riboavin Derivative as a Photosensitizer, *Chemical Engineering Journal*, Vol.355, 2019, pp. 130-136.

[57] Y. F. Wang, F. A. Roddick, L. H. Fan, Direct and Indirect Photolysis of Seven Micropollutants in Secondary Effluent from a Wastewater Lagoon, *Chemosphere*, Vol.185, 2017, pp. 297-308.

[58] Z. H. Xu, C. Y. Jing, F. S. Li, X. G. Meng, Mechanisms of Photocatalytical Degradation of

Monomethylarsonic and Dimethylarsinic Acids using Nanocrystalline Titanium Dioxide, *Environmental Science & Technology*, Vol.42, 2008, pp. 2349-2354.

[59] X. D. Xie, Z. C. Zhang, Y. N. Hu, H. F. Cheng, A Mechanistic Kinetic Model for Singlet Oxygen Mediated Self Sensitized Photo-Oxidation of Organic Pollutants in Water, *Chemical Engineering Journal,* Vol.334, 2018, pp. 1242-1251.

Contribution of Individual Authors to the Creation of a Scientific Article (Ghostwriting Policy)

Prof. Dr. Delia Teresa Sponza and Post-Dr. Rukiye Öztekin took an active role in every stage of the preparation of this article.

The authors equally contributed in the present research, at all stages from the formulation of the problem to the final findings and solution.

Sources of Funding for Research Presented in a Scientific Article or Scientific Article Itself

The experimental phases of this research study were conducted at the National Research Council (NRC) of Canada, Research Centers, Ontario, Canada. The authors would like to thank this body for providing financial support.

Conflict of Interest

The authors have no conflicts of interest to declare that are relevant to the content of this article.

Creative Commons Attribution License 4.0 (Attribution 4.0 International, CC BY 4.0)

This article is published under the terms of the Creative Commons Attribution License 4.0
https://creativecommons.org/licenses/by/4.0/deed.en_US

APPENDIX

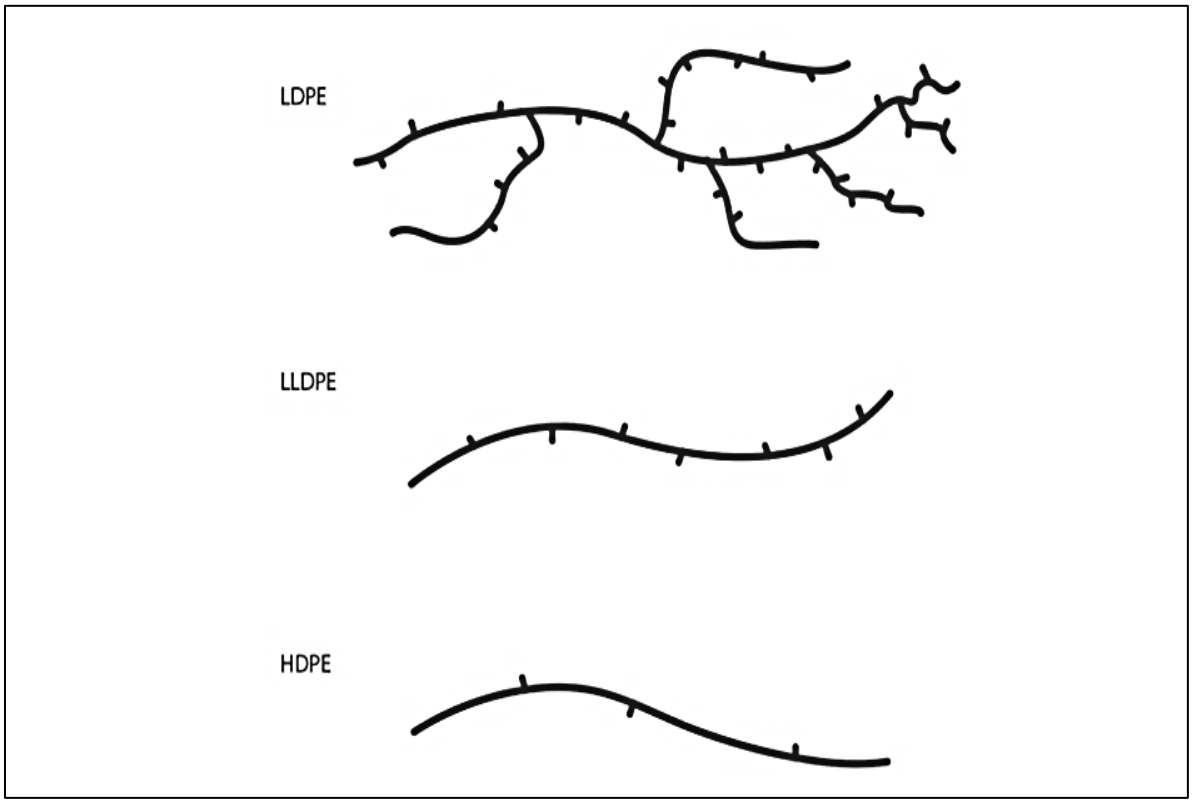


Figure 1. The images of HDPE linear chain

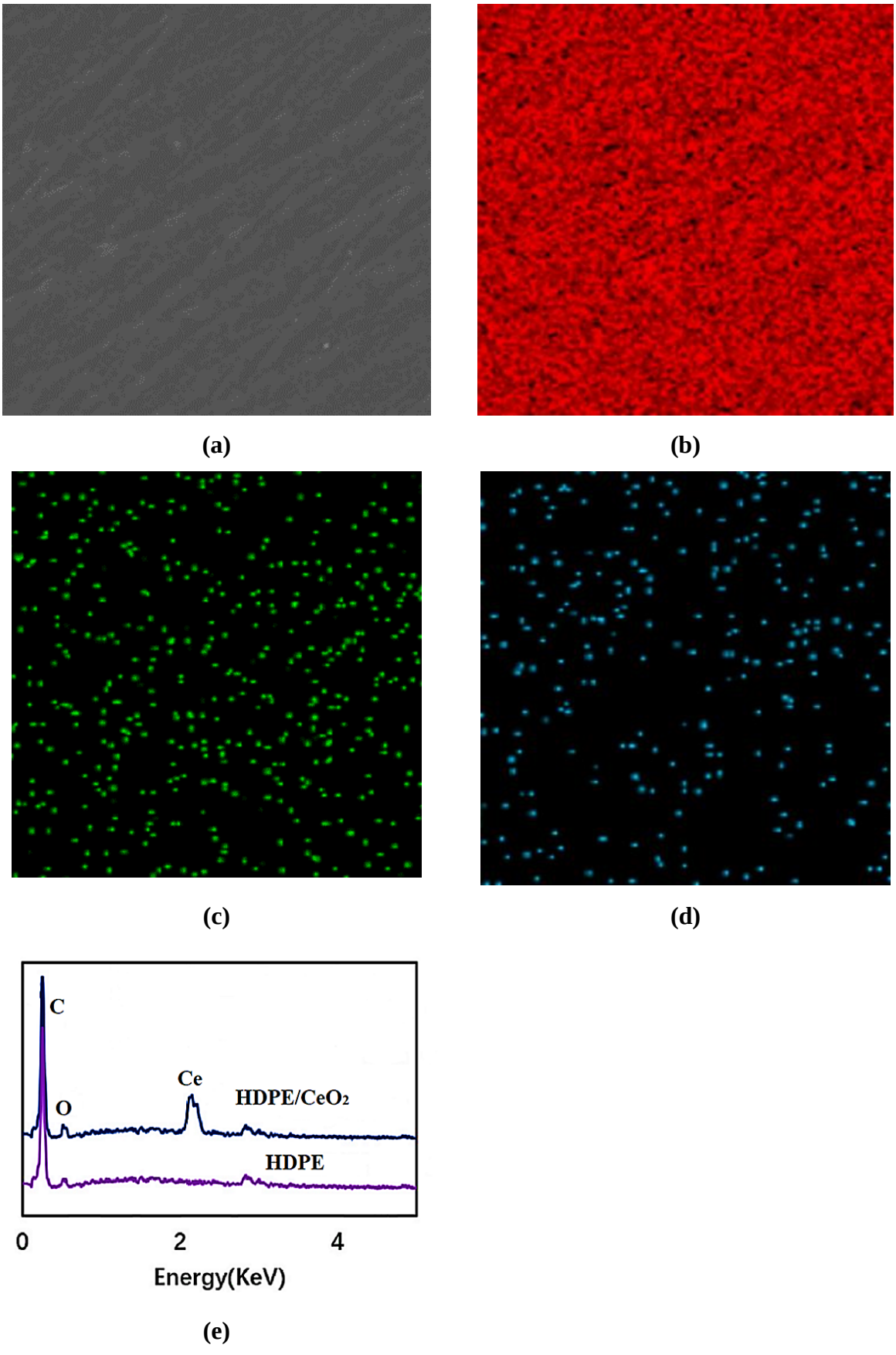
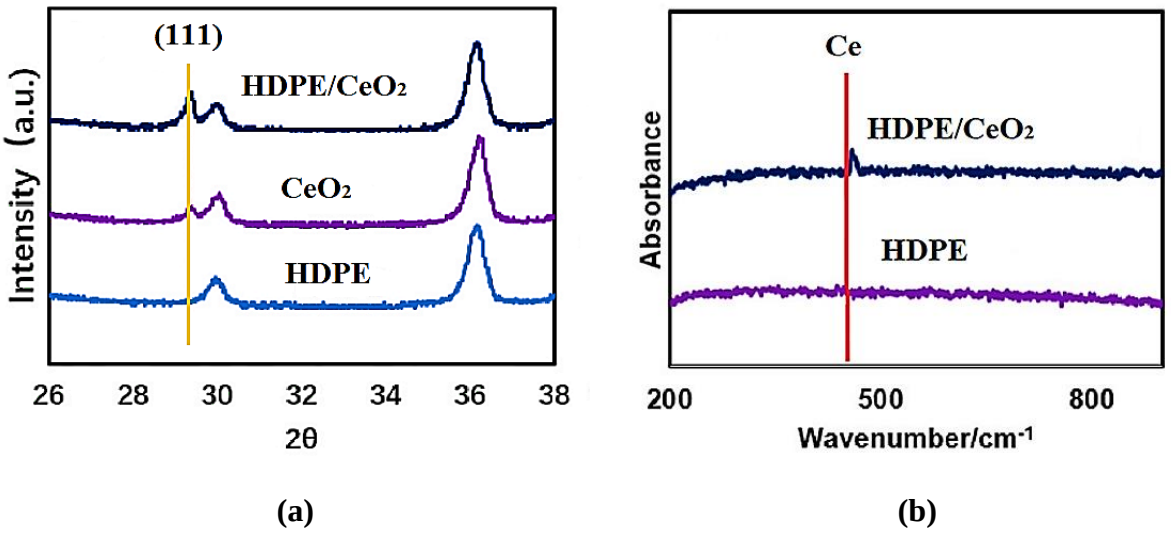


Figure 2. EDS spectra of **(a)** HDPE-CeO_2 NCs **(b)** element C, **(c)** element Ce, **(d)** element O, and **(e)** element contents of HDPE and CeO_2 composites from EDX after PD process, respectively.



(a) **(b)**

Figure 3. The results of HDPE/CeO_2 NCs **(a)** XRD analysis and **(b)** Raman analysis, respectively.

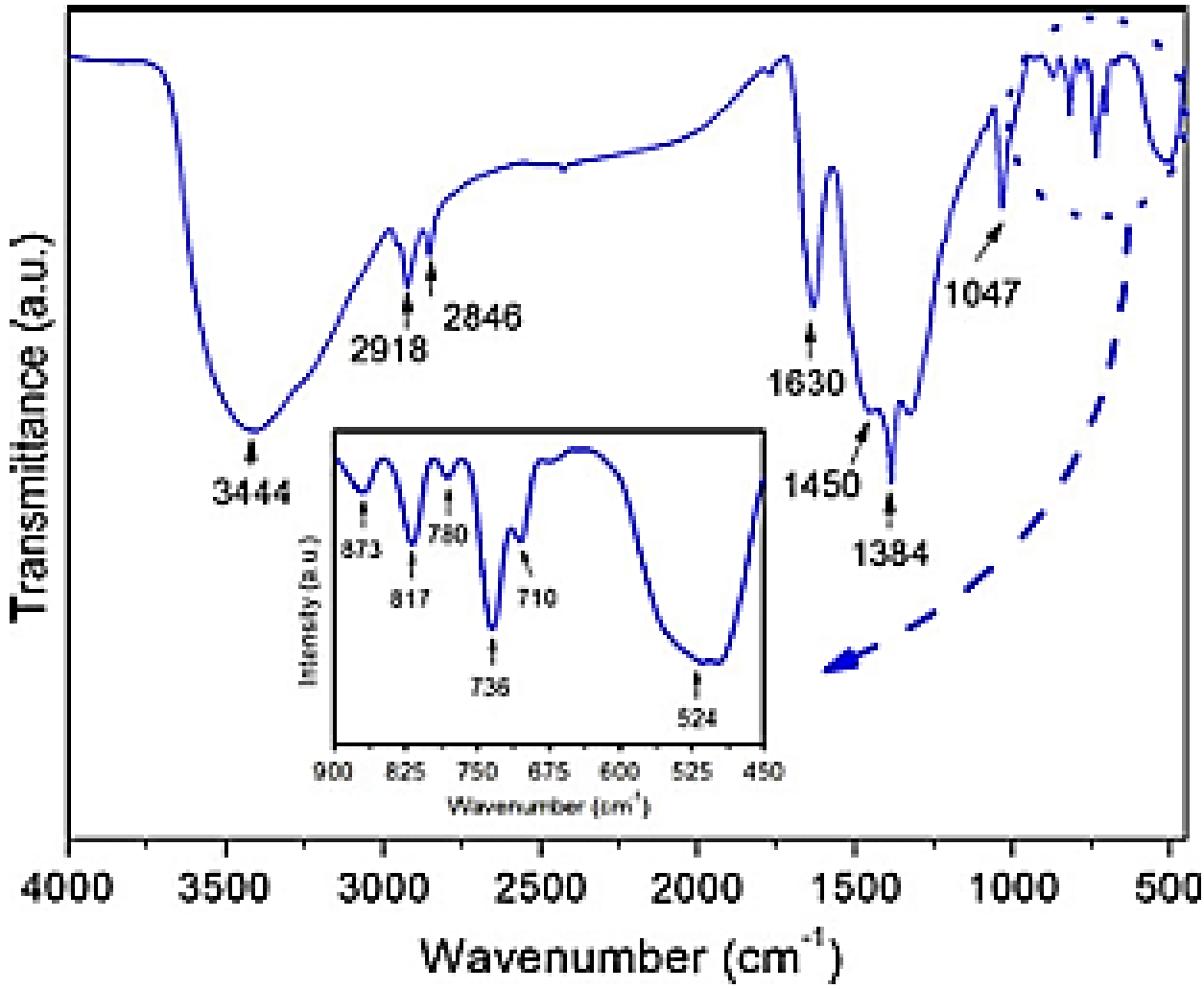
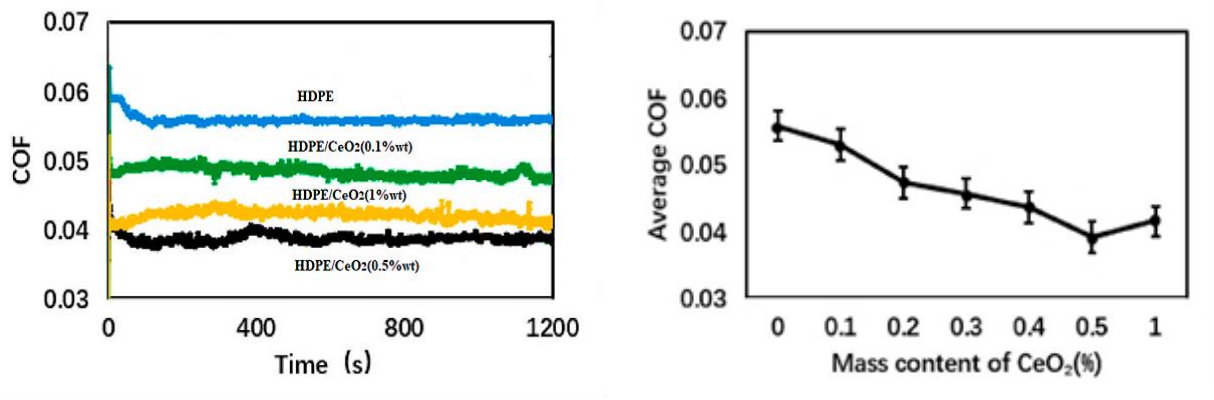


Figure 4. FTIR results HDPE/CeO_2 NCs



(a) **(b)**

Figure 5. The results of COF curves of **(a)** four different HDPE composites [HDPE, HDPE/CeO_2(0.1%wt), HDPE/CeO_2(0.5%wt), CeO_2-HDPE/CeO_2(1%wt), and **(b)** Average COFs of modified HDPE composites with different mass contents of CeO_2, respectively.

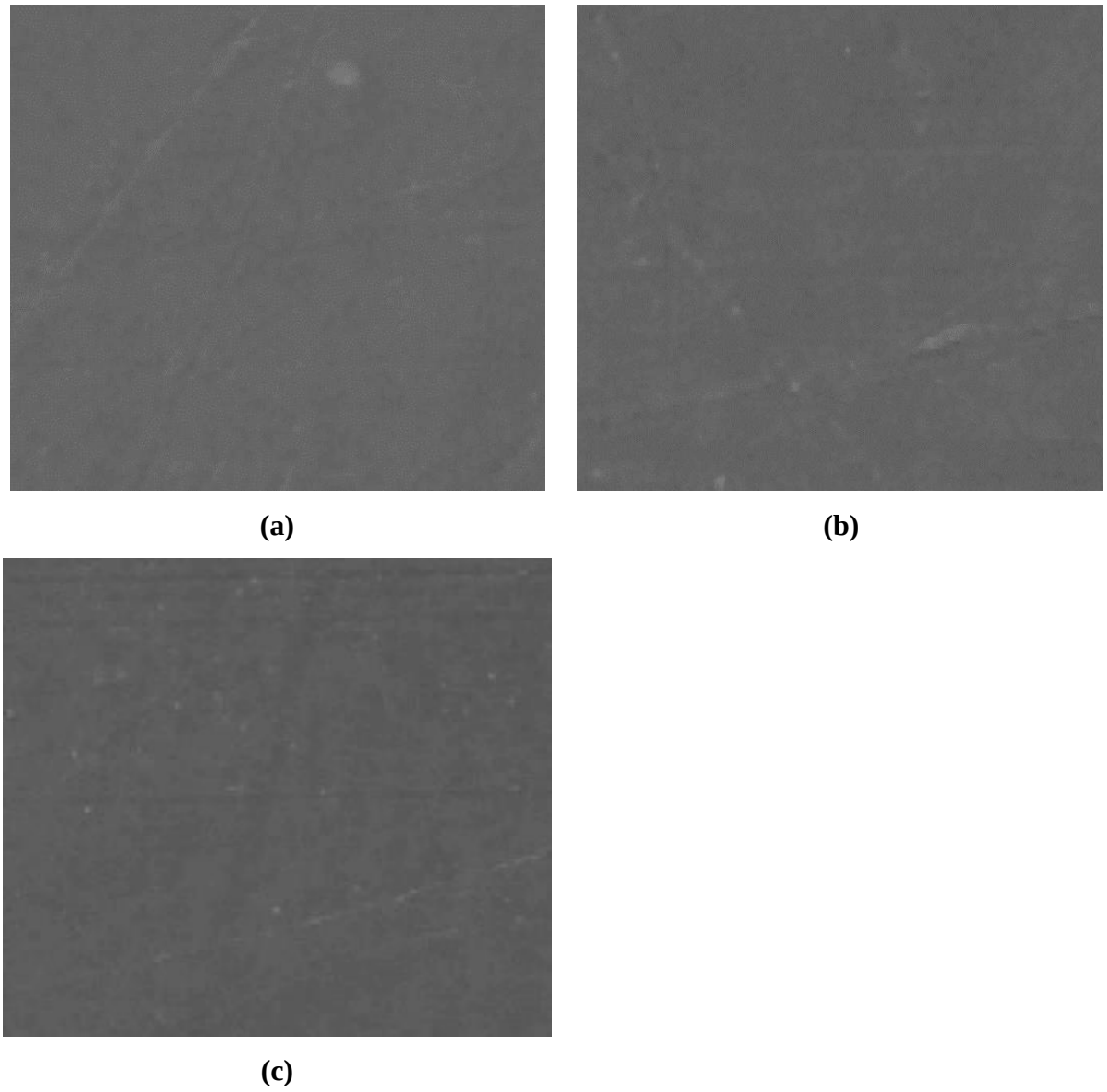


Figure 6. SEM results of HDPE/CeO_2 NCs for the polished surface of HDPE and the surfaces of CeO_2 ball before **(a), (b),** and after **(c)** tribological experiments, respectively. (SEM image size: 100 μm).

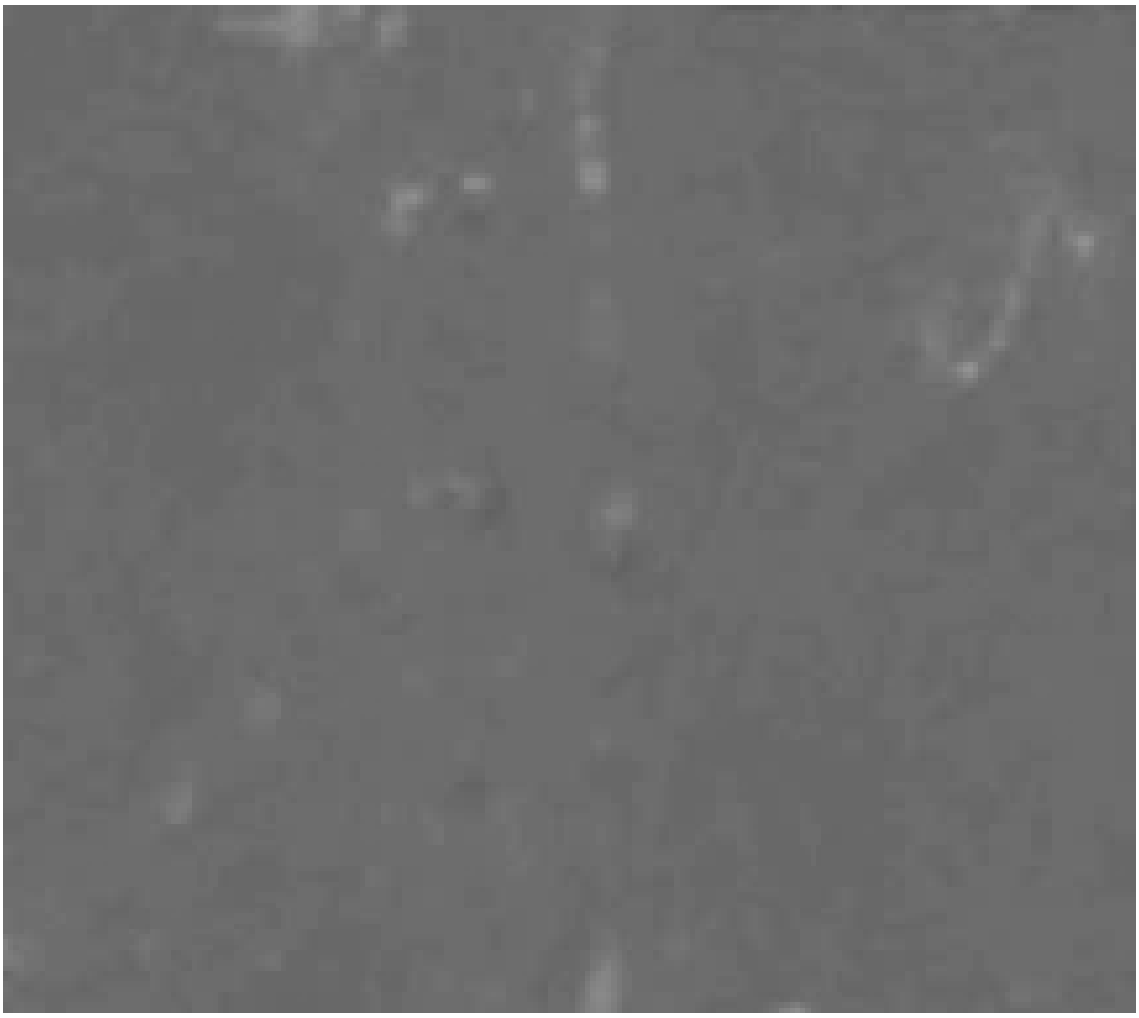


Figure 7. SEM results of HDPE/CeO_2 NCs with an aging test after 20 min of photooxidation time crack. (SEM image size: 100 μm)

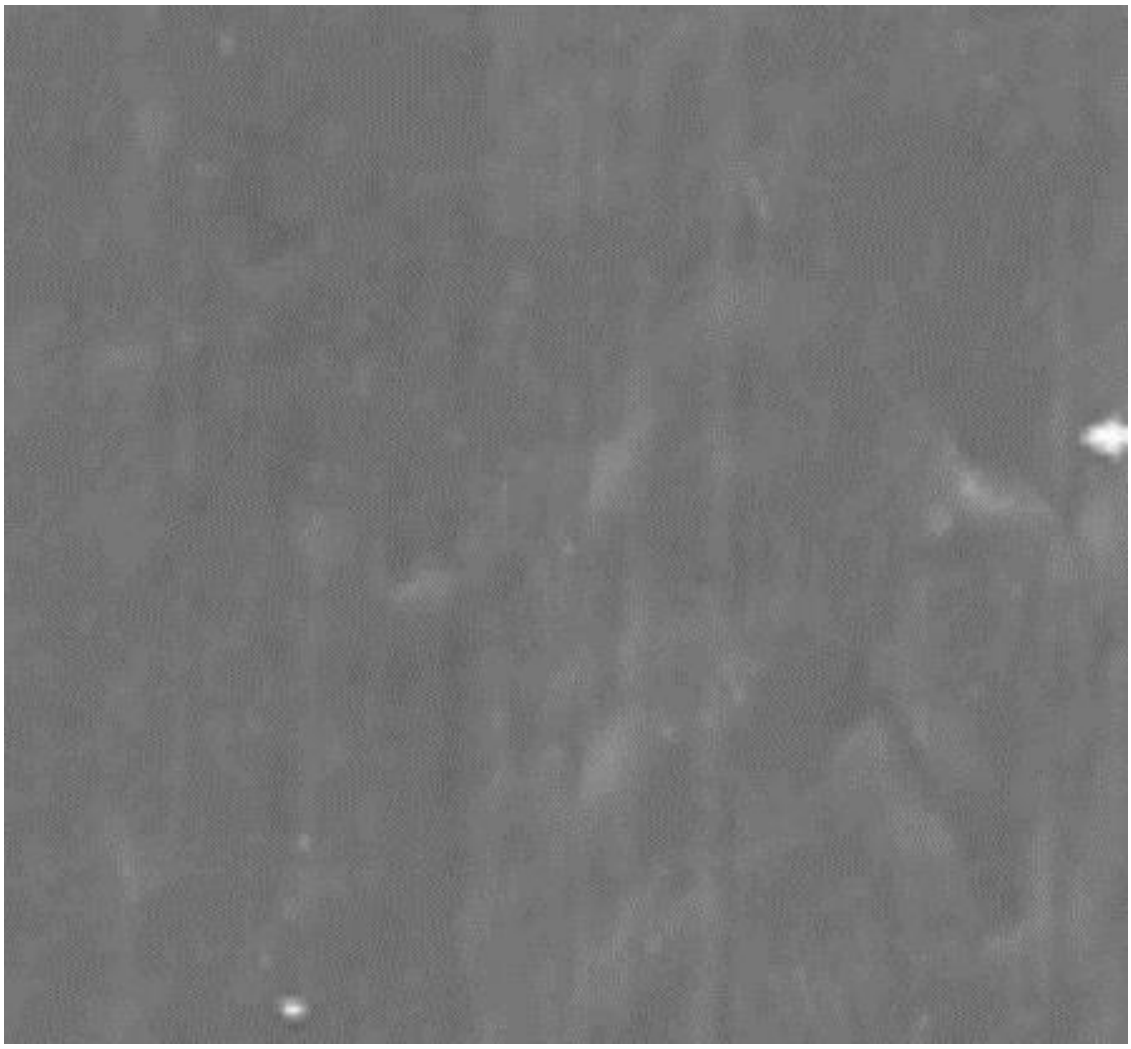


Figure 8. SEM results of HDPE/CeO_2 NCs with as aging test after 40 min photooxidation time, respectively. (SEM image size: 100 μm).

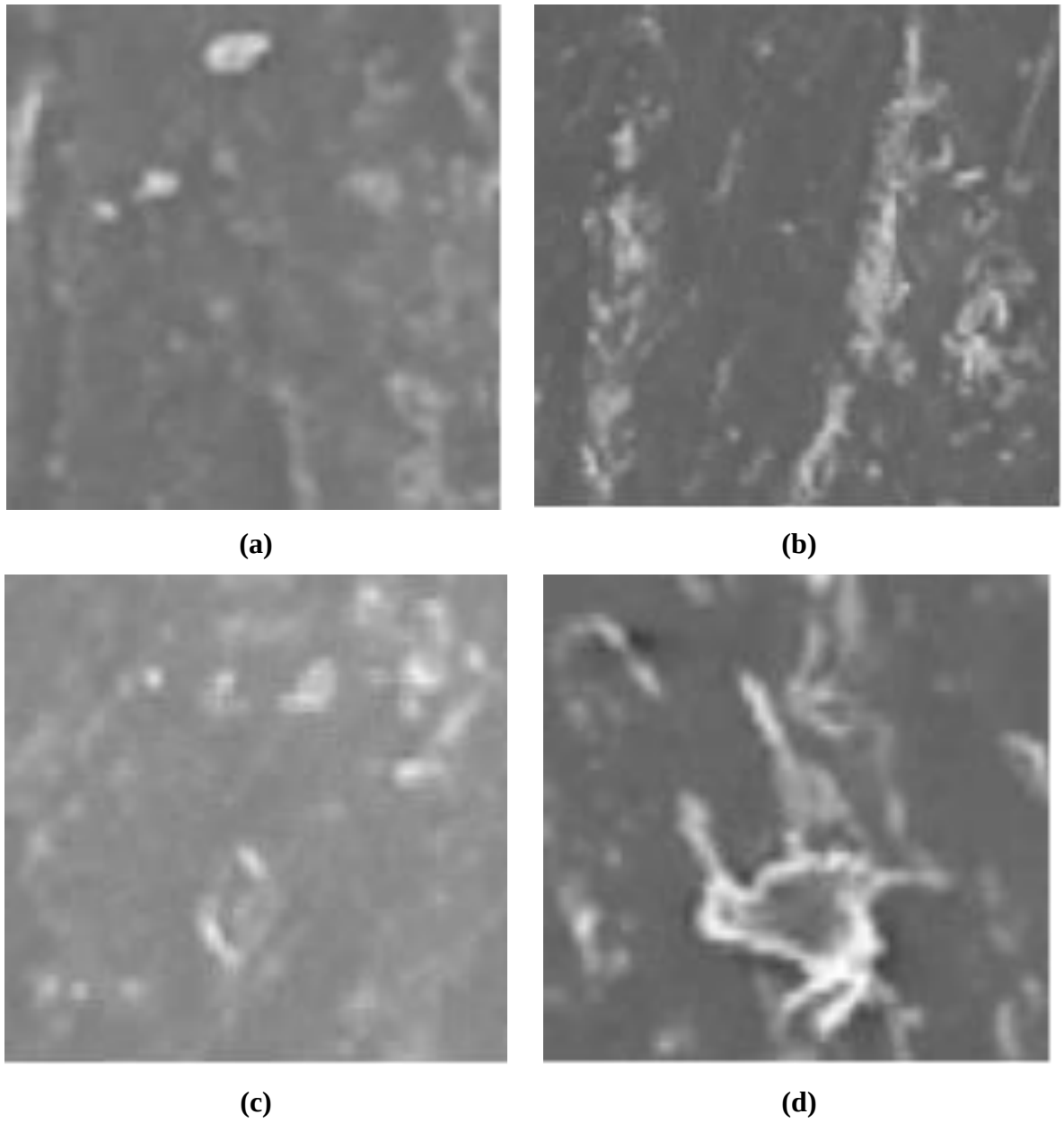


Figure 9. SEM results of HDPE/CeO_2 NCs for the surface deformation of the material after **(a)** 10 min, **(b)** 20 min, **(c)** 30 min, and **(d)** 40 min photooxidation times, respectively. (SEM image size: 100 μm)

Table 1. Operational conditions for ROX with HDPE/CeO_2 NCs under photodegradation process

Parameters	**Operational conditions for ROX with HDPE/CeO_2 NCs under photodegradation process**								
	Units	**Values**							
Sunlight power	W/m^2	20	30	40	50	60	80	100	
Photooxidation time	min	10	30	40	50	60	80	100	
pH		2	4	7	8	10			
Temperature	T°(C)	10	20	25	30	35	40		
Cerium dioxide (CeO_2)	mg/l	2.5	4	8	10	12	14	16	18
HDPE concentrations	mg/l	40	200	300	800	1000	1200	1400	1600
ROX concentration	mg/l	500	600	800	1000	1500	2000	3000	4000
HDPE to CeO_2 ratios		40	50	37.5	80	83.34	100	85.72	88.88
HDPE/CeO_2 concentration	mg/l	200	800	1000	1800	2000	2400		

Table 2. Effect of increasing ROX concentration on the ROX photodegradation yields

ROX concentration (mg/l)	**HDPE concentration (mg/l)**	**CeO_2 concentration (mg/l)**	**HDPE/CeO_2 ratio**	**ROX Removal efficiency (%)**
500	100	2.5	40	96 ± 0.144
600	200	4	50	90 ± 0.135
800	300	8	37.5	99 ± 0.149
1000	800	10	80	89 ± 0.134
1500	1000	12	83.34	85 ± 0.128
2000	1200	14	100	65 ± 0.098
3000	1400	16	85.72	82 ± 0.123
4000	1600	18	88.88	79 ± 0.119

Table 3. Effect of pH on the ROX photodegradation yield

pH	**ROX Removal efficiency (%)**
2.0	69 ± 0.104
4.0	99 ± 0.149
7.0	90 ± 0.135
8.0	45 ± 0.068
10.0	34 ± 0.051

Table 4. Effect of HDPE/CeO_2 ratio on photodegradation of ROX

HDPE concentration (mg/l)	**CeO_2 concentration (mg/l)**	**HDPE/CeO_2 ratio**	**ROX Removal efficiency (%)**
100	2.5	40	96 ± 0.144
200	4	50	90 ± 0.135
300	8	37.5	99 ± 0.149
800	10	80	89 ± 0.134
1000	12	83.34	85 ± 0.128
1200	14	100	65 ± 0.098
1400	16	85.72	82 ± 0.123
1600	18	88.88	79 ± 0.119

Table 5. Effect of increasing HDPE/CeO_2 NCs concentration on the ROX photodegradation yield

HDPE/CeO_2 NCs Concentration (mg/l)	**ROX Removal efficiency (%)**
200	48 ± 0.072
800	59 ± 0.089
1000	70 ± 0.105
1800	84 ± 0.126
2000	99 ± 0.149
2400	96 ± 0.144

Table 6. Effect of sunlight on ROX photodegradation

Sunlight intensity (W/m^2)	**ROX Removal efficiency (%)**
20	79 ± 0.119
30	80 ± 0.120
40	89 ± 0.134
50	92 ± 0.138
60	99 ± 0.149
80	80 ± 0.120
100	80 ± 0.120

Table 7. Effect of photodegradation time on ROX photodegradation

Photodegradation time (min)	**ROX Removal efficiency (%)**
10	95 ± 0.143
30	99 ± 0.149
40	99 ± 0.149
50	98 ± 0.147
60	98 ± 0.147
80	80 ± 0.120
100	80 ± 0.120

Table 8. Effect of temperature on ROX photodegradation

Temperature (°C)	**ROX Removal efficiency (%)**
10	69 ± 0.104
20	76 ± 0.114
25	82 ± 0.123
30	95 ± 0.143
35	97 ± 0.146
40	99 ± 0.149
50	91 ± 0.137
60	80 ± 0.120

Table 9. Langmuir–Hinshelwood constants for ROX photodegradation.

Pollutant	K_{app} **(min^{-1})**	k **(M^{-1})**	**Correlation coefficient**
ROX	12.349×10^{-6}	9.234×10^{-4}	0.9999

Table 10. ANOVA analysis using BBD in RSM for ROX degradation by HDPE/CeO_2 NCs.

Source	Sum of Squares	df	Mean Square	F-value	p-value	Comments	%P
Model	16726.47	14	1194.75	219.42	< 0.0001	significant	
A-pH	1953.61	1	1953.61	358.78	< 0.0001	significant	11.68
B-Conc	1805.6	1	1805.6	331.6	< 0.0001	significant	10.79
C-Time	6444.04	1	6444.04	1183.45	< 0.0001	significant	38.53
D-Dosage	235.79	1	235.79	43.3	< 0.0001		1.41
AB	283.34	1	283.34	52.04	< 0.0001		1.69
AC	17.35	1	17.35	3.19	0.1018	not significant	0.10
AD	0.0927	1	0.0927	0.017	0.8986	not significant	0.00
BC	58.37	1	58.37	10.72	0.0074	significant	0.35
BD	0.06	1	0.06	0.011	0.9183	not significant	0.00
CD	4.06	1	4.06	0.7457	0.4063	not significant	0.02
A^2	1012.05	1	1012.05	185.86	< 0.0001		6.05
B^2	608.2	1	608.2	111.7	< 0.0001		3.64
C^2	2423.75	1	2423.75	445.12	< 0.0001	significant	14.49
D^2	2317.59	1	2317.59	425.63	< 0.0001		13.86
Residual	59.9	11	5.45				
Lack of fit	59.76	10	5.98	44.2	0.1166	not significant	
Pure Error	0.1352	1	0.1352				
Cor Total	16786.37	25					
Std. Dev.	2.33						
Mean = 51.43; C.V.% = 4.54; R^2 = 0.996; Adjusted. R^2 = 0.992; Predicted. R^2 = 0.981; Adeq. Precision = 46.45							

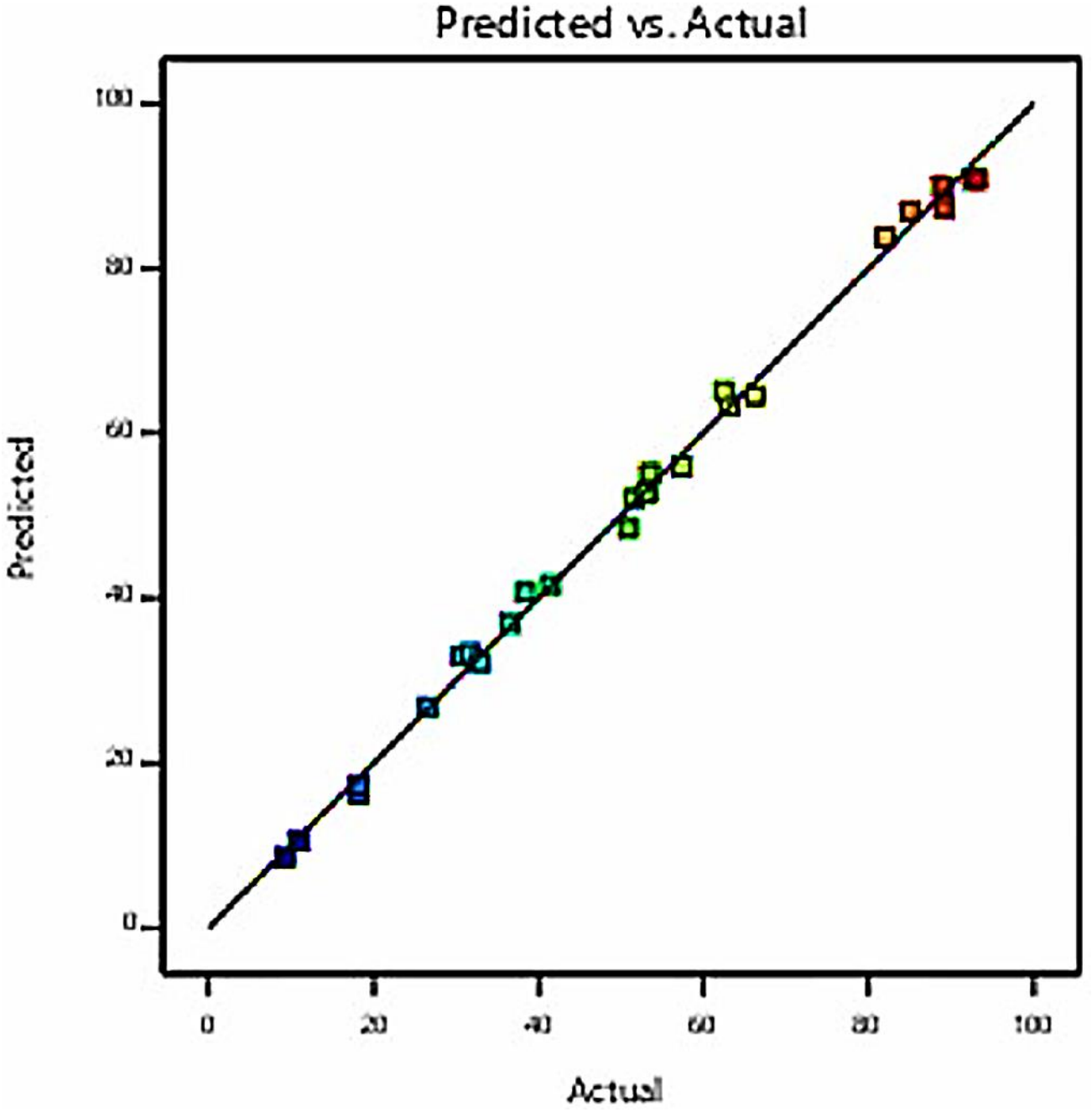


Figure 10. Plot of actual against predicted plot for ROX degradation by HDPE/CeO_2 NCs.

Table 11. Apparent rate constant (k) and standard error (R^2) of the pseudo-first-order kinetics fitting on ROX photodegradation at varying concentration

No		k (h^{-1})	R^2
Sunlight power (W/m^2)	Blank	3.89E-05	4.69E-05
	20	0.00304	5.27E-04
	30	0.00462	8.29E-04
	40	0.01086	1.18E-03
	50	0.01077	1.07E-03
	60	0.01070	0.92E-03
	80	0.01065	0.86E-03
	100	0.01054	0.81E-03
Photooxidation Time (min)	10	0.00315	5.31E-04
	30	0.00467	8.27E-04
	40	0.01081	1.19E-03
	50	0.01075	1.05E-03
	60	0.01070	0.94E-03
	80	0.01058	0.81E-03
	100	0.01052	0.80E-03
Temperature (^oC)	10	0.01086	1.08E-03
	20	0.01089	1.03E-03
	25	0.01512	7.34E-04
	30	0.01625	1.42E-03
	35	0.01753	1.48E-03
	40	0.01760	1.51E-03
pH	2	0.00874	9.88E-04
	4	0.00965	1.06E-03
	7	0.01086	1.18E-03
	8	0.01128	1.35E-03
	10	0.01141	1.62E-03
HDPE concentration (mg/l)	Control	0.01086	1.18E-03
	40	0.01533	1.01E-03
	200	0.02388	1.46E-03
	300	0.04025	2.85E-03
	800	0.04137	2.98E-03
	1000	0.04324	3.01E-03
	1200	0.04750	3.22E-03
	1400	0.04789	3.58E-03
	1600	0.04942	4.04E-03
CeO_2 concentration (mg/l)	Control	0.01086	1.18E-03
	2.5	0.01068	5.51E-03
	4	0.00427	2.14E-04
	8	0.00292	4.32E-04
	10	0.00287	4.51E-04
	12	0.00275	4.78E-04
	14	0.00252	4.93E-04
	16	0.00246	5.02E-04

	18	0.00239	5.14E-04
ROX concentration (mg/l)	500	0.01872	2.58E-03
	600	0.01086	1.18E-03
	800	0.00324	2.02E-04
	1000	6.20E-04	1.15E-05
	1500	7.04E-04	1.29E-05
	2000	7.32E-04	1.34E-05
	3000	7.96E-04	1.37E-05
	4000	8.01E-04	1.45E-05
HDPE/CeO_2 ratios	40	0.01878	2.61E-03
	50	0.01089	2.27E-03
	37.5	0.00331	2.42E-04
	80	6.22E-04	1.19E-05
	83.34	7.10E-04	1.31E-05
	100	7.38E-04	1.39E-05
	85.72	7.99E-04	1.46E-05
	88.88	8.05E-04	1.55E-05
HDPE/CeO_2 NCs Concentration (mg/l)	200	0.00312	5.33E-04
	800	0.00461	8.24E-04
	1000	0.01086	1.17E-03
	1800	0.01073	1.03E-03
	2000	0.01079	0.91E-03
	2400	0.01055	0.86E-03

Table 12. Training data

Sample	Time(h)	ROX (mg/l)	Sunlight power (W/m^2)	T (℃)	HDPE (mg/l)	pH	CeO_2 (mg/l)	HDPE/CeO_2 ratio	Degradation
1	10	500	60	40	300	4	8	37.5	1
2	30	500	60	40	300	4	8	37.5	0.75023
3	40	500	60	40	300	4	8	37.5	0.6053
4	50	500	60	40	300	4	8	37.5	0.54082
5	60	500	60	40	300	4	8	37.5	0.50742
6	80	500	60	40	300	4	8	37.5	0.45324
7	100	500	60	40	300	4	8	37.5	0.43678
8	10	1000	60	40	300	4	8	37.5	1
9	30	1000	60	40	300	4	8	37.5	0.82846
10	40	1000	60	40	300	4	8	37.5	0.77587
11	50	1000	60	40	300	4	8	37.5	0.72376
12	60	1000	60	40	300	4	8	37.5	0.67411
13	80	1000	60	40	300	4	8	37.5	0.62457
14	100	1000	60	40	300	4	8	37.5	0.61541
15	10	4000	60	40	300	4	8	37.5	1
16	30	4000	60	40	300	4	8	37.5	0.98432
17	40	4000	60	40	300	4	8	37.5	0.94787
18	50	4000	60	40	300	4	8	37.5	0.92042
19	60	4000	60	40	300	4	8	37.5	0.89998
20	80	4000	60	40	300	4	8	37.5	0.88547
21	100	4000	60	40	300	4	8	37.5	0.87120
22	10	800	60	40	300	4	8	37.5	1
23	30	800	60	40	300	4	8	37.5	0.99432
24	40	800	60	40	300	4	8	37.5	0.99043
25	50	800	60	40	300	4	8	37.5	0.985
26	60	800	60	40	300	4	8	37.5	0.98023
27	80	800	60	40	300	4	8	37.5	0.97523
28	100	800	60	40	300	4	8	37.5	0.97014
29	10	600	100	30	1000	7	12	40	1
30	30	600	100	30	1000	7	12	40	0.93028
31	40	600	100	30	1000	7	12	40	0.92897
32	50	600	100	30	1000	7	12	40	0.9073
33	60	600	100	30	1000	7	12	40	0.88502
34	80	600	100	30	1000	7	12	40	0.87334
35	100	600	100	30	1000	7	12	40	0.86360
36	10	1500	80	25	1400	7	16	80	1
37	30	1500	80	25	1400	7	16	80	0.90765
38	40	1500	80	25	1400	7	16	80	0.87156
39	50	1500	80	25	1400	7	16	80	0.86621
40	60	1500	80	25	1400	7	16	80	0.8262

41	80	1500	80	25	1400	7	16	80	0.81792
42	100	1500	80	25	1400	7	16	80	0.80975
43	10	2000	50	25	800	8	14	83.34	1
44	30	2000	50	25	800	8	14	83.34	0.8463
45	40	2000	50	25	800	8	14	83.34	0.77207
46	50	2000	50	25	800	8	14	83.34	0.73948
47	60	2000	50	25	800	8	14	83.34	0.68366
48	80	2000	50	25	800	8	14	83.34	0.62457
49	100	2000	50	25	800	8	14	83.34	0.61758
50	10	3000	40	25	1200	10	18	85.72	1
51	30	3000	40	25	1200	10	18	85.72	0.84354
52	40	3000	40	25	1200	10	18	85.72	0.77554
53	50	3000	40	25	1200	10	18	85.72	0.73542
54	60	3000	40	25	1200	10	18	85.72	0.67411
55	80	3000	40	25	1200	10	18	85.72	0.64570
56	100	3000	40	25	1200	10	18	85.72	0.63786
57	10	1000	80	40	1600	7	10	88.88	1
58	30	1000	80	40	1600	7	10	88.88	0.80723
59	40	1000	80	40	1600	7	10	88.88	0.66473
60	50	1000	80	40	1600	7	10	88.88	0.63151
61	60	1000	80	40	1600	7	10	88.88	0.55566
62	80	1000	80	40	1600	7	10	88.88	0.47368
63	100	1000	80	40	1600	7	10	88.88	0.45893
64	10	800	60	25	1000	8	4	100	1
65	30	800	60	25	1000	8	4	100	0.80537
66	40	800	60	25	1000	8	4	100	0.73920
67	50	800	60	25	1000	8	4	100	0.70266
68	60	800	60	25	1000	8	4	100	0.64099
69	80	800	60	25	1000	8	4	100	0.61153
70	100	800	60	25	1000	8	4	100	0.60908
71	10	1500	100	25	200	2	2.5	50	1
72	30	1500	100	25	200	2	2.5	50	0.82193
73	40	1500	100	25	200	2	2.5	50	0.75626
74	50	1500	100	25	200	2	2.5	50	0.72445
75	60	1500	100	25	200	2	2.5	50	0.67718
76	80	1500	100	25	200	2	2.5	50	0.60252
77	100	1500	100	25	200	2	2.5	50	0.59871
78	10	500	40	25	300	4	8	80	1
79	30	500	40	25	300	4	8	80	0.86212
80	40	500	40	25	300	4	8	80	0.78448
81	50	500	40	25	300	4	8	80	0.76852
82	60	500	40	25	300	4	8	80	0.71347
83	80	500	40	25	300	4	8	80	0.65536

84	100	500	40	25	300	4	8	80	0.64268
									0.63450
85	10	600	60	25	800	7	10	83.34	1
86	30	600	60	25	800	7	10	83.34	0.86157
87	40	600	60	25	800	7	10	83.34	0.80704
88	50	600	60	25	800	7	10	83.34	0.78345
89	60	600	60	25	800	7	10	83.34	0.73123
90	80	600	60	25	800	7	10	83.34	0.68033
91	100	600	60	25	800	7	10	83.34	0.67910
92	10	800	50	25	1000	8	12	100	1
93	30	800	50	25	1000	8	12	100	0.8713
94	40	800	50	25	1000	8	12	100	0.76481
95	50	800	50	25	1000	8	12	100	0.68109
96	60	800	50	25	1000	8	12	100	0.60105
97	80	800	50	25	1000	8	12	100	0.51917
98	100	800	50	25	1000	8	12	100	0.50784
99	10	1000	30	25	1200	10	14	85.72	1
100	30	1000	30	25	1200	10	14	85.72	0.76416
101	40	1000	30	25	1200	10	14	85.72	0.63555
102	50	1000	30	25	1200	10	14	85.72	0.51436
103	60	1000	30	25	1200	10	14	85.72	0.42922
104	80	1000	30	25	1200	10	14	85.72	0.38717
105	100	1000	30	25	1200	10	14	85.72	0.37659
106	10	1500	20	25	1400	2	16	88.88	1
107	30	1500	20	25	1400	2	16	88.88	0.6901
108	40	1500	20	25	1400	2	16	88.88	0.45437
109	50	1500	20	25	1400	2	16	88.88	0.34282
110	60	1500	20	25	1400	2	16	88.88	0.23527
112	80	1500	20	25	1400	2	16	88.88	0.21177
113	100	1500	20	25	1400	2	16	88.88	0.20985
114	10	2000	80	25	1600	4	18	80	1
115	30	2000	80	25	1600	4	18	80	0.93171
116	40	2000	80	25	1600	4	18	80	0.85305
117	50	2000	80	25	1600	4	18	80	0.76013
118	60	2000	80	25	1600	4	18	80	0.73196
119	80	2000	80	25	1600	4	18	80	0.65051
120	100	2000	80	25	1600	4	18	80	0.62754
121	10	3000	100	25	200	7	2.5	50	1
122	30	3000	100	25	200	7	2.5	50	0.97663
123	40	3000	100	25	200	7	2.5	50	0.9
124	50	3000	100	25	200	7	2.5	50	0.85
125	60	3000	100	25	200	7	2.5	50	0.78
126	80	3000	100	25	200	7	2.5	50	0.75
127	100	3000	100	25	200	7	2.5	50	0.77

128	10	4000	60	25	40	8	12	37.5	1
129	30	4000	60	25	40	8	12	37.5	0.97663
130	40	4000	60	25	40	8	12	37.5	0.92694
131	50	4000	60	25	40	8	12	37.5	0.90527
132	60	4000	60	25	40	8	12	37.5	0.86969
133	80	4000	60	25	40	8	12	37.5	0.84783
134	100	4000	60	25	40	8	12	37.5	0.82350
135	10	800	40	25	300	10	8	80	1
136	30	800	40	25	300	10	8	80	0.92739
137	40	800	40	25	300	10	8	80	0.89809
138	50	800	40	25	300	10	8	80	0.86989
139	60	800	40	25	300	10	8	80	0.85320
140	80	800	40	25	300	10	8	80	0.82528
141	100	800	40	25	300	10	8	80	0.81780
142	10	600	20	25	800	7	14	100	1
143	30	600	20	25	800	7	14	100	0.66608
144	40	600	20	25	800	7	14	100	0.55272
145	50	600	20	25	800	7	14	100	0.48417
146	60	600	20	25	800	7	14	100	0.45818
147	80	600	20	25	800	7	14	100	0.43009
148	100	600	20	25	800	7	14	100	0.42769

Table 13. Validating data

Sample	Time	ROX	Sunlight power	T (ºC)	HDPE	pH	CeO_2	HDPE/CeO_2 ratios	HDPE/CeO_2 NCs
1	10	800	60	40	300	4	8	37.5	2000
2	30	800	60	40	300	4	8	37.5	2000
3	40	800	60	40	300	4	8	37.5	2000
4	50	800	60	40	300	4	8	37.5	2000
5	60	800	60	40	300	4	8	37.5	2000
6	80	800	60	40	300	4	8	37.5	2000
7	100	800	60	40	300	4	8	37.5	2000
8	10	800	60	40	300	4	8	37.5	2000
9	30	800	60	40	300	4	8	37.5	2000
10	40	800	60	40	300	4	8	37.5	2000
11	50	800	60	40	300	4	8	37.5	2000
12	60	800	60	40	300	4	8	37.5	2000
13	80	800	60	40	300	4	8	37.5	2000
14	100	800	60	40	300	4	8	37.5	2000
15	10	800	60	40	300	4	8	37.5	2000
16	30	800	60	40	300	4	8	37.5	2000
17	40	800	60	40	300	4	8	37.5	2000
18	50	800	60	40	300	4	8	37.5	2000
19	60	800	60	40	300	4	8	37.5	2000
20	80	800	60	40	300	4	8	37.5	2000
21	100	800	60	40	300	4	8	37.5	2000
22	10	800	60	40	300	4	8	37.5	2000
23	30	800	60	40	300	4	8	37.5	2000
24	40	800	60	40	300	4	8	37.5	2000
25	50	800	60	40	300	4	8	37.5	2000
26	60	800	60	40	300	4	8	37.5	2000
27	80	800	60	40	300	4	8	37.5	2000
28	100	800	60	40	300	4	8	37.5	2000
29	10	800	60	40	300	4	8	37.5	2000
30	30	800	60	40	300	4	8	37.5	2000
31	40	800	60	40	300	4	8	37.5	2000
32	50	800	60	40	300	4	8	37.5	2000
33	60	800	60	40	300	4	8	37.5	2000
34	80	800	60	40	300	4	8	37.5	2000
35	100	800	60	40	300	4	8	37.5	2000